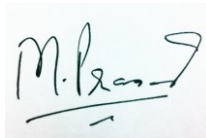**DOE Award No.: DE-FE-0009963**

Quarterly Research Performance Progress Report (Period ending 09/30/2015)

Measurement and Interpretation of Seismic Velocities and Attenuations in Hydrate-Bearing Sediments

Project Period (10/1/2012 to 9/30/2015)

Submitted by:
co-PI: Manika Prasad
Colorado School of Mines
DUNS #010628170.
1500 Illinois Street
Golden. CO 80401
e-mail: mprasad@mines.edu
Phone number: (303) 273-3457
Submission Date: 4/30/2015

Prepared for:
United States Department of Energy
National Energy Technology Laboratory

Office of Fossil Energy

Disclaimer

This report was prepared as an account of work sponsored by an agency of the United States Government. Neither the United States Government nor any agency thereof, nor any of their employees, makes any warranty, express or implied, or assumes any legal liability or responsibility for the accuracy, completeness, or usefulness of any information, apparatus, product, or process disclosed, or represents that its use would not infringe privately owned rights. Reference herein to any specific commercial product, process, or service by trade name, trademark, manufacturer, or otherwise does not necessarily constitute or imply its endorsement, recommendation, or favoring by the United States Government or any agency thereof. The views and opinions of authors expressed herein do not necessarily state or reflect those of the United States Government or any agency thereof.

Abstract

Measurement and Interpretation of Seismic Velocities and Attenuations
in Hydrate-Bearing Sediments

Grant/Cooperative Agreement DE-FE 0009963.

During this period we performed low frequency measurements on Fox Hills sandstone as part of an interlaboratory comparison study. We hope to achieve the following:

- Decrease the process of sample preparation

- Developing a baseline for our up-coming low frequency measurements that will include the same sandstone with the presence of hydrates

- A direct comparison between two low frequency setups – This will give us a better idea about the quality of the recorded data

We performed Micro-CT measurements under pressure. The test was performed to prove that we can visually observe changes induced by confining pressure (reduction in porosity, breaking of grains). The pressure control system in combination with ultrasonic transducers will allow to visually observe pore scale changes in gas hydrate bearing sediments while simultaneously identifying the hydrates' influence on ultrasonic velocities.

We have started redesigning an experimental setup to study methane hydrate formation in sediments. The setup is capable of maintaining high pressures (approximately 1500 psi or 10.34 MPa) and a range of temperatures (from -5 °C to 20 °C). At this stage, the setup has been constructed and installed. In the next quarter (Q13), we will perform pressure leak tests and calibrations before conducting any experiments in the setup.

Finally, we have submitted two papers to the Journal "Geophysical Prospecting" which are currently under review (Attached separately).

Table of Contents

List of Figures and Tables

List of Figures

List of Tables

2. Accomplishments

2.1 Overview of Milestone Status

Our current position is shown by a red bar in the Gantt chart in Figure 1. The Milestone status is shown in Table 1. In the current period of Q12 (Q4 of Year 3), we continued our work on Task 9 – MXCT Characterization. We worked on attenuation properties of hydrates forming out of solution (Task 7). This is fundamental work which will be used for Task 11 – Comparison with Log Data.

We requested and got approval for a no-cost extension of the project until April 30, 2016. This extension will allow us to catch up for setbacks in our progress on CH4 hydrates. A post-doctoral scholar, Dr. Ahmad A.A.Majid has joined the group. Dr. Majid has experience in making CH4 hydrates and has redesigned his old setup for our experiments.

Students: Ms. Mandy Schindler is scheduled to defend her thesis proposal in the coming quarter (Q13).
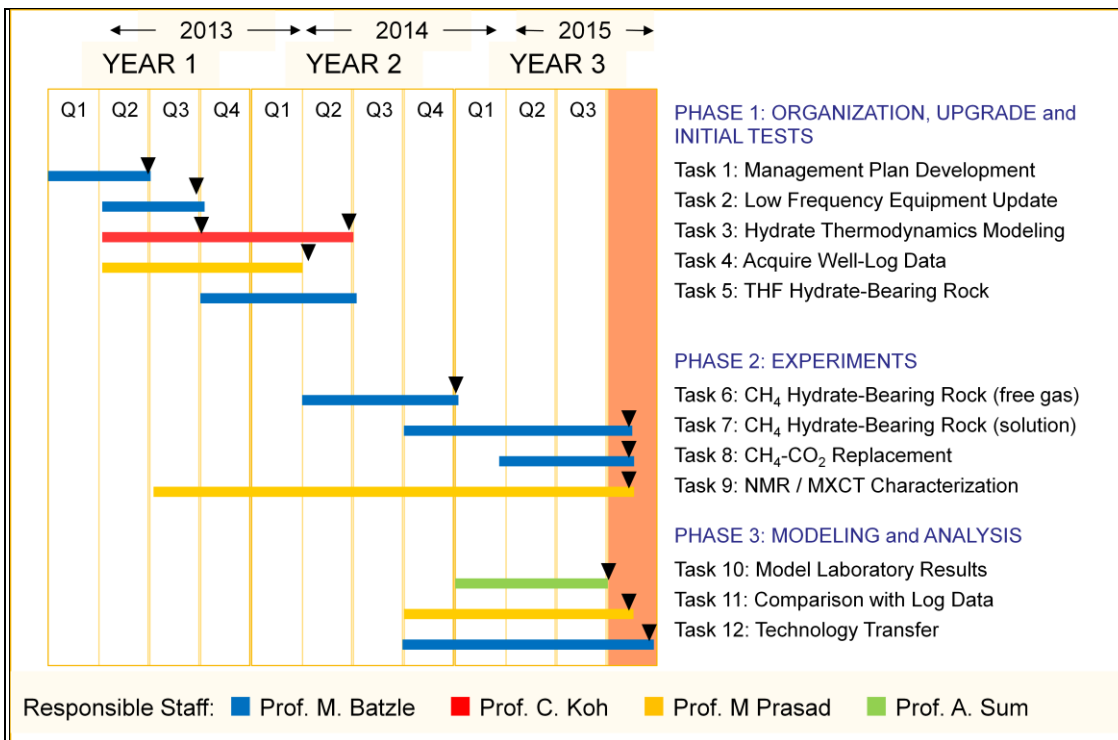
Figure 1: Gantt chart showing milestones and current status.

Table 1: Milestone status

Mile-stone	Task	Title / Description	Status	Completion date (completed or expected)
Completed				
1	1	Project Management Plan (PMP)	Complete & approved	1 Dec 2012
2	2	Modifications to low frequency system	Completed	1 June 2013
3	3	Modeling established using EOS	Completed	31 May 2014
4	3	Property models of hydrates completed	Completed	31 May 2014
5	4	Logs acquired and database established	Completed	15 Jun 2014
6	5	THF hydrate grown in pressure vessel	Completed	15 Apr 2014
7	6	Methane hydrates from free gas phase (somewhat behind schedule)	Continuing*	31 Dec 2015
Continuing or Planned				
8	7	Methane hydrates from gas in solution	Started	30 Jun 2016
9	8	CO2 replacing methane in hydrates	Planned**	30 Jun 2016
10	9	MXCT scans conducted	Continuing*	31 Mar 2016
11	10	Effective media models complete	Continuing	31 Mar 2016
12	11	Comparison to in situ data complete	Planned	30 Jun 2016
13	12	Information Dissemination	Continuing*	30 Jun 2016
*initial stages were completed on schedule, but the process continues throughout the project				
** if methane hydrate formation is successful				

2.2 Low Frequency Measurements

During this period, Mr. Mathias Pohl conducted low frequency measurements at SINTEF in Trondheim, Norway as part of an interlaboratory comparison study. The goal of this comparison study is to compare low frequency measurements performed here at Colorado School of Mines with experiments over in Trondheim.

We hope to adopt some of the sample preparation steps to decrease our sample preparation time. At the same time, we hope to improve data reliability and repeatability by a comparative study of data collected with similar techniques at different laboratories. In Q12 and Q13, we will expand this laboratory comparison to other research groups as well.

Note: This research exchange and travel is funded by the ROSE project but we hope to use the obtained results for our low frequency measurements on hydrate bearing sediments which we will start in the next quarter.

2.2.1 CSM Measurements

The low-frequency measurement itself is based on the linear stress-strain relationship (Hooke's law). By knowing the exerted stress applied on the sample and the resulting deformation we are able to calculate Young's modulus, Poisson's ratio, bulk modulus, shear modulus, and compressional modulus. By knowing these elastic constants at each measured frequency we can calculate its corresponding compressional (p) and shear (s) wave velocities.

Here at CSM, the sample preparation is a tedious and most of all time consuming process. After the sample is cut into a cylindrical shape (usally 1 inch or 1 and 1/2 inch) it is covered with a thin layer of K20 which is sandpapered down to achieve a smooth sample surface. This layer of K20 depends on the roughness of the sample. Additionally a thin layer of kapton is glued on the outside of the sample which helps prevent fluid leakage. Onto this layer of kapton we glue our strain gages. The next step is to glue aluminium end caps to the top and bottom of the sample. These end caps serve two purposes. They are used to indirectly calculate the applied stress, as well as they are used for ultrasonic velocity measurements. To prevent further leakage an additional layer of kapton is glued onto the sample covering parts of the transducers. The sample then is covered with a layer of soft epoxy to seal it and to avoid the penetration of the confining gas into the sample.

Once all of these steps are done, it is installed into the measurement assembly by gluing the bottom part of the sample to the shaker and the top part to the top of the assembly. This assembly is then lowered into a pressure vessel. Fluid ports allow fluid injection into the sample. One digital pump is used to control the pore pressure. The confining pressure was applied using nitrogen gas. A uniaxial sinusoidal stress at discrete frequencies (2-2000 Hz) is applied by a shaker on the bottom of the sample. A function generator produced a signal which drives the shaker. The strain gages then measured the resulting strains.

2.2.2 SINTEF Measurements

The low-frequency measurements at SINTEF are also based on the linear stress-strain relationship (Hooke's law).

However, the sample preparation and assembly process is significantly less time consuming. Again, after the sample is cut into a cylindrical shape depending of the roughness of the sample it needs to be covered with a thin layer of K20 which is then sandpapered down to a smooth surface. Instead of applying a layer of kapton onto the sample the strain gages are directly placed onto the sample. They are hold in place by simply using scotch tape. A rubber sleeve is put over the sample and strain gages. This rubber sleeve prevents leakage into the sample. On the top part of the sample it is sealed by an o-ring and on the bottom part vulcanizing tape where the wires from the strain gages come out. After this step the sample is ready to be put into a pressure vessel.

Because the sample itself is not glued to the bottom or top part of the stack a uniaxial stress needs to be applied to guarantee a good contact between all of the parts. This uniaxial stress always needs to be bigger than the applied confining stress. The confining pressure fluid is lamp oil.

The limitation of this setup is the confining pressure itself. As stated before, the strain gages are not glued onto the sample. A confining pressure needs to be applied so that the strain gages are pressed against the sample. After applying a sinusoidal excitation of the sample the friction between the sample and the strain gages is big enough to cause a measurable signal.

Saturated Measurements:
Two different pore fluids were used during the experiments. In the following we are going to present the low frequency measurement results for FoxHill 4 (oil saturated) and FoxHill 5 (DI-water saturated).

Oil Saturated
Figure 2 shows the measured Poisson's Ratio for FoxHill 4. It is noticeable that after saturation the Poisson's Ratio increases. Also, by opening and closing the pore fluid lines we were able to observed the drained and undrained effect, allowing the pore fluid to flow in and out of the sample (drained). This effect is only observable up to around 10 Hz, above that critical frequency the drained and undrained values are identical.
Figure 3 shows the calculated compressional and shear wave velocity for FoxHill 4. Again the drained and undrained effect can be seen. Also, by saturating the sample with oil the compressional velocity increases whereas the shear wave velocity decreases.

Figure 2: Average Poisson's Ratio for FoxHill 4. Comparison between the moduli in the dry stage and after saturation. The Red squares were measured while the pore fluid lines were open (Drained) and the Blue squares were measured while the pore fluid lines were closed (Un-drained)

Figure 3: Average velocities for FoxHill 4. Comparison between the compressional wave velocity dry and oil saturated as well as the shear wave velocity dry and saturated.

DI-Water Saturated

Figure 4 shows the measured Poisson's Ratio for FoxHill 5 before and after saturating it with DI-water. It can be seen that we were able to observe the drained and undrained effect but the measured Poisson's Ratio values for the saturated sample are above 0.4. This drastic increase in Poisson's Ratio is unreasonable. It results from the measured

strains from the radial gages. We are in the process of looking for answers that can explain this increase in Poisson's Ratio.

Figure 5 shows the corresponding compressional and shear wave velocities. Due to this extremely high measured Poisson's Ratio the compressional wave velocities are over calculated. Nevertheless, the shear wave velocities seem to be in agreement with our expectations.
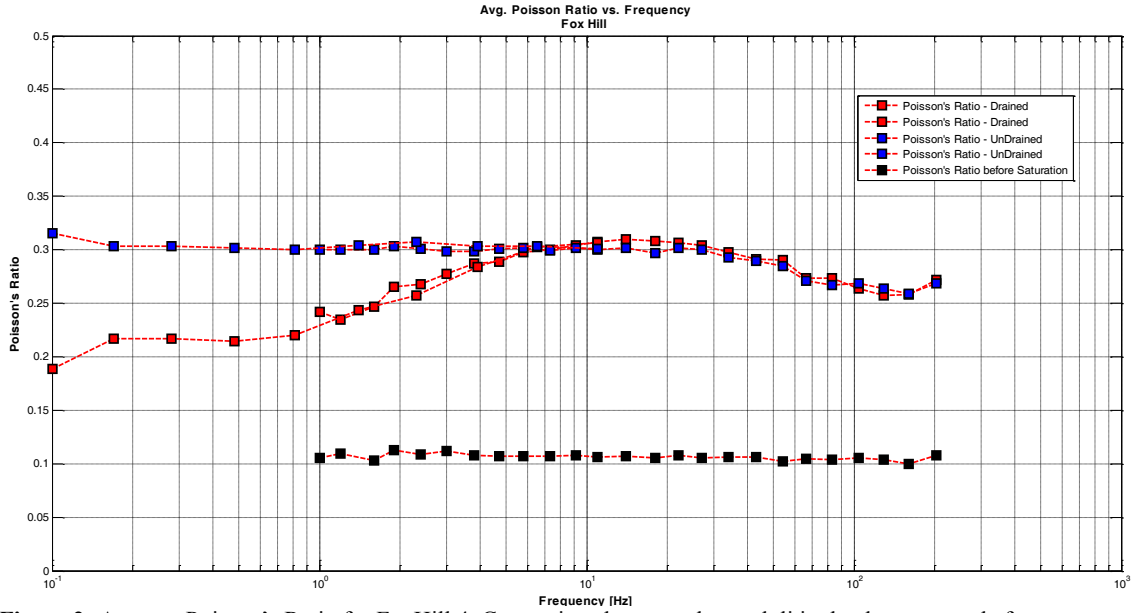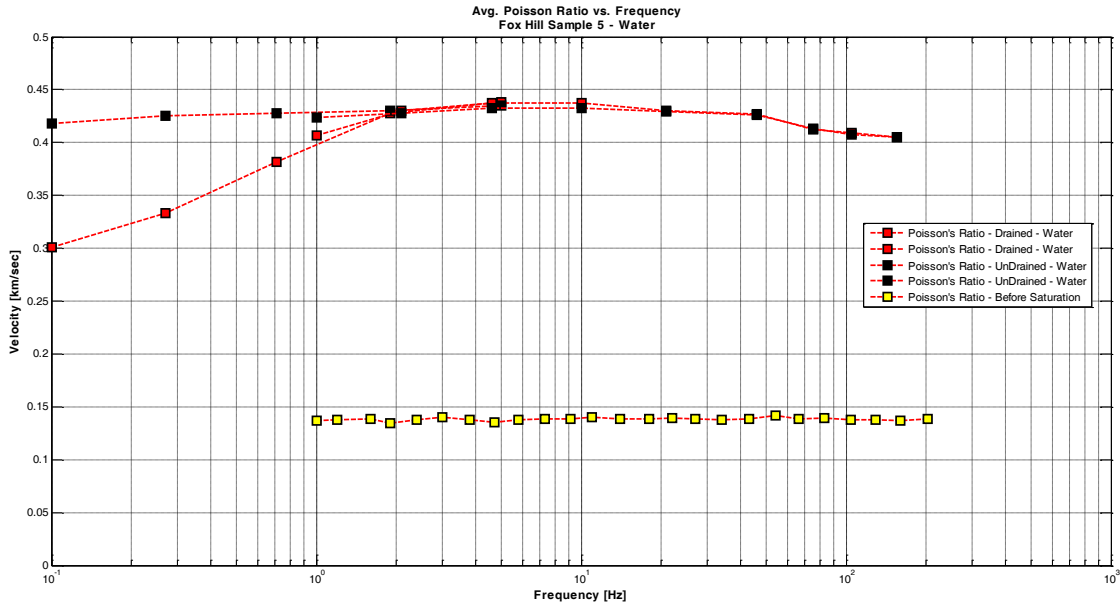

Figure 4: Average Poisson's Ratio for FoxHill 5. Comparison between the moduli in the dry stage and after saturation. The Red squares were measured while the pore fluid lines were open (Drained) and the Black squares were measured while the pore fluid lines were closed (Un-drained).
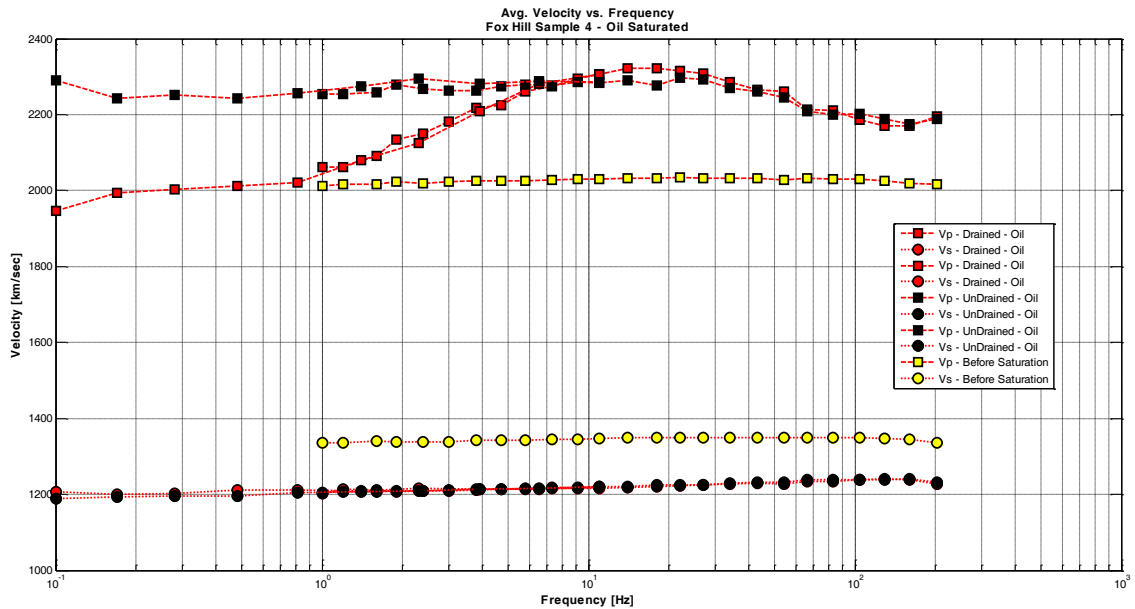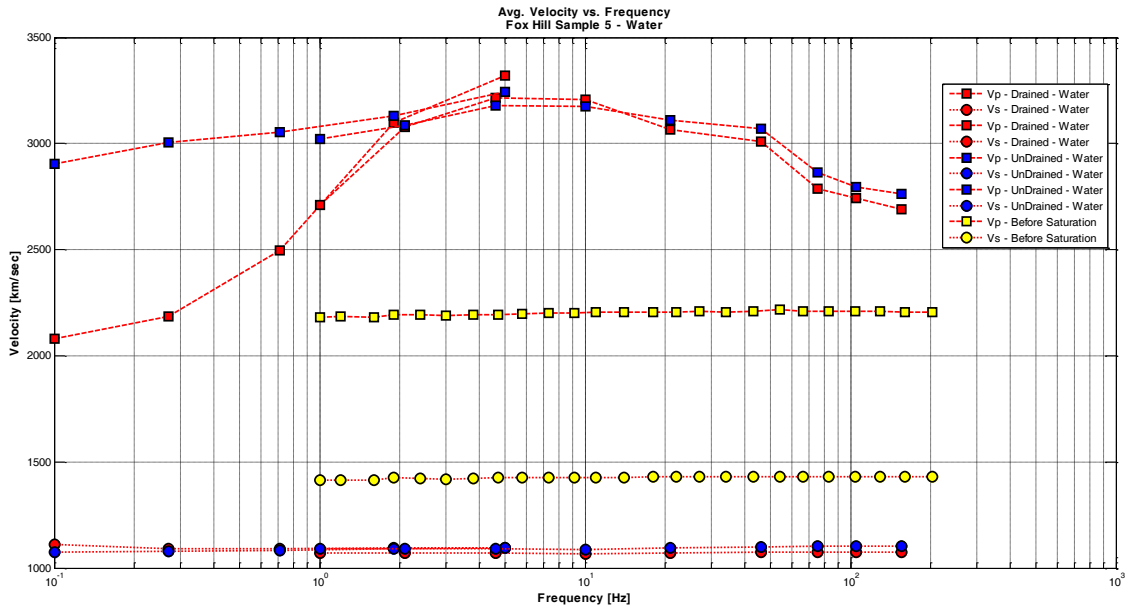

Figure 5: Average velocities for FoxHill 5. Comparison between the compressional wave velocity dry and DI-water saturated as well as the shear wave velocity dry and saturated.

2.2.3 Preliminary Results

In this report we presented the first part of our interlaboratory comparison study. Our results from the measurements obtained at SINTEF show that we can obtain representative data for the dry samples. The oil saturated sample shows explainable increases in the compressional wave velocities and an decrease in the shear wave velocities. However, the results obtained for sample saturated with DI-water are not explainable at this point and require further interpretation.

2.3 Micro CT Imaging under Confining Pressure

We are implementing a pressure and temperature control system that can be used inside the Xradia-400 micro CT machine in order to perform micro CT imaging on methane hydrate bearing sediments.

The temperature control and ultrasonic transducers have been introduced in previous reports. In Q12, we ran test scans on jacketed rock samples under confining pressure inside the micro CT machine. Figure 1 depicts the setup inside the micro CT scanner.

Figure 6: Big (1-inch outer diameter) Torlon[®] pressure vessel in micro CT machine with tubing and valve for pressurization.

The tested samples have been jacketed with heat-shrink tubing and consisted of aluminum pieces on both ends and quartz sand, glass beads and Bentheim sandstone

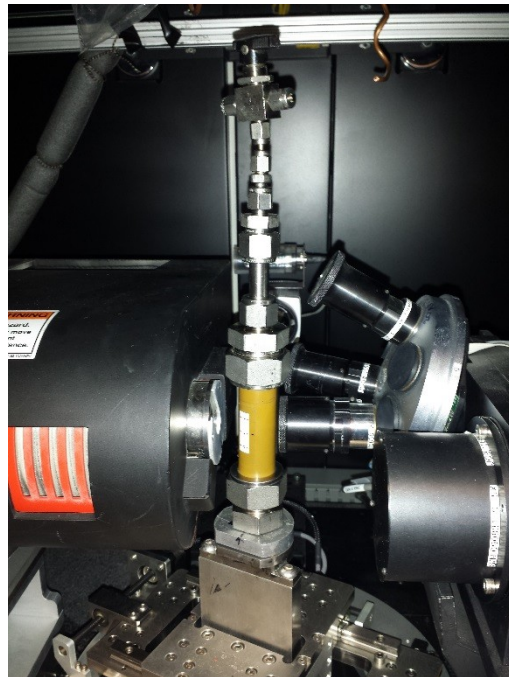samples in between (Figure 6). The samples were clamped with pieces of wire for additional sealing of the heat-shrink layer. The samples were approximately 12 cm long and had a diameter of 1.2 cm. The samples were placed in the big Torlon vessel (1-inch outer diameter). The confining pressure of 1500 psi was applied through an ISCO pump with water as confining fluid. The pressurization was done outside of the CT scanner, a valve was used to keep the vessel pressurized throughout the scanning process (Figure 6).

Figure 7: Sample jacketed in heat shrink tubing. The tested samples consisted of aluminum cylinders on both ends and quartz sand, sandstone or glass beads in between

We performed 5 test scans on samples of different materials (Bentheim Sandstone, quartz sand, quartz sand with bentonite, glass beads) under confining pressure. The samples were jacketed with heat-shrink tubing. The pore space was filled with air. Figure 8 shows a coarse grained quartz sand sample under atmospheric pressure and 1500 psi (10.3 MPa) confining pressure. The comparison between both images shows a compaction of the sample. A reduction of porosity from 37.6% to 31.2% was determined from the images. Further, significant damage to the grains was observed. Previously intact grains show cracks after confining pressure was applied (Figure 8 b). The test was performed to prove that we can visually observe changes induced by confining pressure.
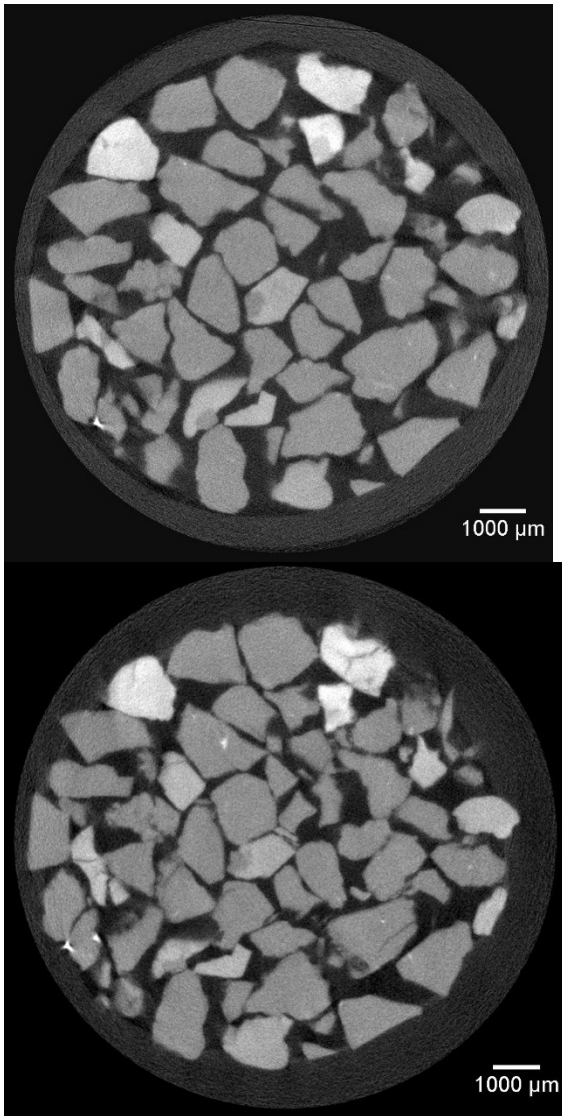
Figure 8: Quartz sand sample at atmospheric pressure and at 1500 psi confining pressure. The images demonstrate a reduction of porosity and damage of the grains due to confining pressure

The pressure control system in combination with ultrasonic transducers will allow to visually observe pore scale changes in gas hydrate bearing sediments while simultaneously identifying the hydrates' influence on ultrasonic velocities.

We are currently working on feed-throughs for fluid lines and electric wiring to use ultrasonic transducers, pressure control and temperature control in combination.

2.4 Experiments on Methane hydrate formation in sediments

In this work, an experimental setup to study methane hydrate formation in sediments was designed and constructed. The setup is capable of operating at high pressures (approximately 1500 psi or 10.34 MPa) and over a range of temperatures (from -5 °C to 20 °C). The setup consists of (1) a high-pressure ISCO pump (1000 HL series with a maximum operating pressure of 2000 psi), (2) a stainless steel experimental reactor cell, 170 ml in volume, (3) an external refrigerated, recirculating chiller, and (4) a cooling bath for fine temperature control. At this stage, the setup has been constructed and installed (Figure 9). The next step will be to perform pressure leak tests and calibrations before performing any experiments in the setup.

Figure 9: Schematic diagram of the experimental setup of the system.

Figure 10: Image of the pressure controls in the experimental setup.
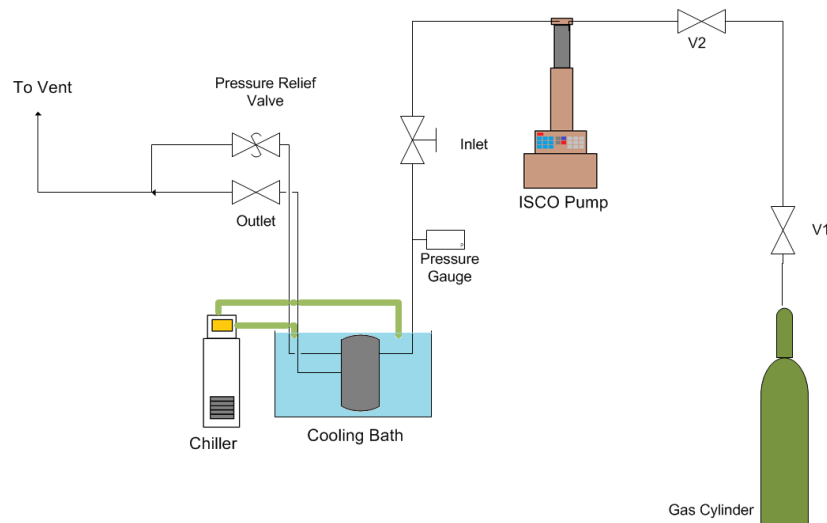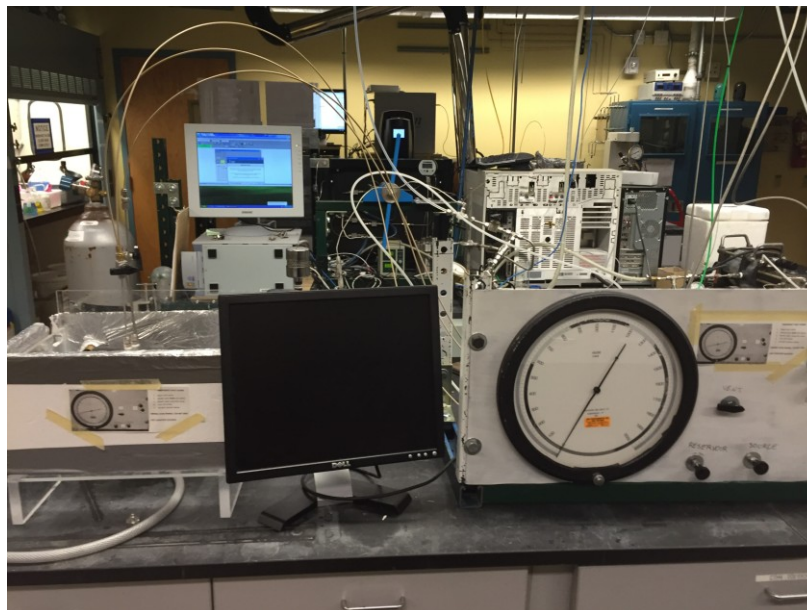
Figure 9 above shows the schematic diagram of the experimental setup. The schematics in Figure 9 and the image in Figure 10 shows the setup consists of a high-pressure ISCO pump, a stainless steel experimental cell, a chiller and a cooling bath. The experimental cell is placed in the cooling bath to control the temperature of the system. In this setup, a coolant (glycol) is circulated into the cooling bath using the chiller to control the temperature. The experimental cell is also connected to the ISCO pump to maintain the pressure of the system at up to 1500 psig (103.4 bar). Currently, the pressure cell comprises two different outlet lines. The first outlet line connects to an outlet valve that is used to vent the system. The second outlet line connects to a pressure relief that will open if the pressure of the cell exceeds a certain set pressure. Additionally, the setup is connected to a gas cylinder that is located in a gas cabinet.

2.4.1. Proposed Experimental Procedures

The experimental procedures for gas hydrate formation using this setup are outlined below.

Hydrate Formation

1. Add the sample to the experimental cell.
2. Properly seal the experimental cell ensuring that it is gas tight.
3. Open Valves V1 and V2 to allow gas to flow from the gas cylinder to the setup.
4. Slowly pressurize the setup by opening the inlet valve.
5. Set the ISCO Pump to operate at a constant pressure mode.
6. Turn on the chiller to the desired temperature.

End of Experiment

The experimental procedures for ending an experiment are outlined below.

1. Turn of the chiller.
2. Turn of the ISCO pump.
3. Slowly depressurize the system by opening the vent valve.
4. Dispose any chemical in the proper container and according to the CSM Waste handling procedures.

2.4.2. Emergency Shut Down Procedure

In the case of an emergency, the following steps (also depicted in Figure 11) have been outlined for safe shut down of the equipment.

1. Turn off the chiller
2. Turn off the ISCO pump
3. Slowly vent the system by opening the vent valve.

Figure 11: Image of the emergency shutdown procedure as marked in the experimental setup.

2.4.3. Current Status of the Equipment

At this stage, the setup has been installed. A Pressure leak test and calibrations need to be conducted before performing any experiments using the setup.

The updates on this setup were reviewed by the CSM team (Prof. Koh, Prof. Prasad, Dr. Majid, Ms. Schindler, and Mr. Pohl). The experimental setup slides prepared by Dr. Majid are reproduced below in Figure 12.

Figure 12: Image of the emergency shutdown procedure as marked in the experimental setup.

3. Acknowledgments

4. Plans

Table 2 shows the Milestones and Deliverables for this quarter. We plan to focus on CH4 hydrates in both, low frequency measurements and MXCT scanning. We are delayed in Milestone 7. However, due to various delays in our experimentation and initial attempts failing to form methane out of the free gas phase, we have a no-cost extension for a more realistic completion date of 4/30/2016.

Table 2. Q12 Milestones and Deliverables

Milestone	Task	Description	Completion date	Report Content
7	6	Methane hydrates from free gas phase (delayed)	03/31/2016	Progress report
10	9	MXCT measurements under pressure	12/31/2015	Progress report
13	12	Information Dissemination	04/30/2016	Progress report
7	6	Low Frequency Measurements	04/30/2016	Progress report

5. Products

Publications (Publications; Conference Papers, Presentations, Books)

Two papers have been submitted to the Journal of Geophysical Prospecting and are currently under review. They are attached separately to this quarterly report.

Website or other Internet sites
http://crusher.mines.edu/CRA-DOE-Hydrates

Technologies or techniques
Nothing to report

Inventions, patent applications and/or licenses
Nothing to report

Other Products
Nothing to report

6. Participants and Collaborating Organizations

CSM personnel:

Name:	Manika Prasad
Project Role:	Principle Investigator
Nearest person month worked this period:	0.25
Contribution to Project:	Dr. Prasad helped with acoustic and attenuation measurements.
Additional Funding Support:	Academic faculty
Collaborated with individual in foreign country:	No
Country(ies) of foreign collaborator:	N/A
Travelled to foreign country:	Yes
If traveled to foreign country(ies),	India, Norway, Germany, Houston

Duration of stay:	1 months

Name:	Michael Batzle
Project Role:	Principle Investigator
Nearest person month worked this period:	
Contribution to Project:	Dr. Batzle was responsible for the overall (dis)organization of the project.
Additional Funding Support:	Academic faculty
Collaborated with individual in foreign country:	No
Country(ies) of foreign collaborator:	N/A
Travelled to foreign country:	No
If traveled to foreign country(ies),	N/A
Duration of stay:	N/A

Name:	Carolyn Koh
Project Role:	Principle Investigator
Nearest person month	0.25

worked this period:	
Contribution to Project:	Dr. Koh helped with CH4 hydrate experimental setup and measurements.
Additional Funding Support:	Academic faculty
Collaborated with individual in foreign country:	No
Country(ies) of foreign collaborator:	N/A
Travelled to foreign country:	Yes
If traveled to foreign country(ies),	N/A
Duration of stay:	N/A

Name:	**Weiping Wang**
Project Role:	Laboratory Manager
Nearest person month worked this period:	1
Contribution to Project:	Mr. Wang assisted in equipment fabrication
Additional Funding Support:	DHI/Fluids consortium, Chinese Mining University
Collaborated with individual in foreign country:	No
Country(ies) of foreign collaborator:	N/A
Travelled to foreign country:	Yes
If traveled to foreign country(ies):	China
duration of stay: N/A:	3 weeks

Name:	**Mathias Pohl**
Project Role:	Ph.D. student
Nearest person month worked this period:	3
Contribution to Project:	Mr. Pohl prepared samples and collected low frequency data.
Additional Funding Support:	N/A
Collaborated with individual in foreign country:	Yes

Country(ies) of foreign collaborator:	Norway
Travelled to foreign country:	Yes
If traveled to foreign country(ies)	Norway
duration of stay:	6 weeks

Name:	**Mandy Schindler**
Project Role:	Ph.D. student
Nearest person month worked this period:	3
Contribution to Project:	Ms. Schindler prepared samples and collected CT data.
Additional Funding Support:	N/A
Collaborated with individual in foreign country:	No
Country(ies) of foreign collaborator:	N/A
Travelled to foreign country:	No
If traveled to foreign country(ies),	N/A
duration of stay:	N/A

Name:	**Ahmad Afif Abdul Majid**
Project Role:	Post Doctoral scholar
Nearest person month worked:	1
Contribution to Project:	Dr. Majid helped setting up our experiment to form methane hydrates out of free gas
Additional Funding Support:	Center for Hydrate Research
Collaborated with individual in foreign country:	No
Country(ies) of foreign collaborator:	N/A
Travelled to foreign country:	No
If traveled to foreign country(ies):	N/A
duration of stay:	N/A

External Collaborations:

Dr. Tim Collett
US Geologic Survey
Denver, Colorado

Support: Dr. Collett provided data and guidance on interpretation and application. He continues to publish numerous papers on hydrate properties.

7. Changes / Problems

1. We requested and got approval for a no-cost extension of the project until April 30, 2016. This extension will allow us to catch up for setbacks in our progress on CH4 hydrates.

2. A post-doctoral scholar, Dr. Ahmad A.A.Majid has joined the group. Dr. Majid has experience in making CH4 hydrates and has redesigned his old setup for our experiments.

3. Once CH4 hydrates have been successfully formed in sediments, we will use the same setup to replace methane hydrates with CO2 hydrates

8. Special Reporting Requirements

None

9. Budgetary Information

Attached separately

Ultrasonic Attenuation of Pure THF-Hydrate

Mathias Pohl[a], Manika Prasad[a] & Michael L. Batzle[a†]

[a]*Colorado School of Mines, Golden, CO, 80401; mpohl@mines.edu*

Abstract

Whether natural gas hydrates are considered a potential gas resource, a geo-hazard, or climate changing factor, the amount of gas hydrates occurring in the subsurface needs to be estimated. To better understand seismic- and acoustic–wave attenuation effects observed in gas hydrate-bearing sediments, we performed ultrasonic velocity measurements on pure tetrahydrofuran (THF) hydrates. For comparison, we also measured velocities through pure water and frozen samples. Our results show an increase in attenuation after hydrate formation, which was caused by a small amount of residual water residing in thin spaces between hydrate grains. We observed a decreased peak frequency in the frequency spectrum, as well as a drop in peak-to-peak amplitude for the ultrasonic waveforms. Our results also show that when samples of THF hydrate were subsequently cooled below the freezing point of water, the frequency content of the waveforms increased again. This frequency increase was accompanied by a velocity increase, suggesting the sample had become completely solid with no residual fluids. This solidification was also observed with NMR measurements, which showed no measurable free hydrogen content within the frozen samples. Comparing the frequency content of these frozen samples with pure water shows great similarity and suggests that the attenuation of a sample that is made up almost entirely of THF hydrate and some ice is comparable to the sample of pure water.

Introduction

Gas hydrates are ice-like crystalline solids which entrap guest molecules (e.g. methane) in water cages (Sloan & Koh, 2008). The occurrence of natural gas hydrates in nature can be detected by an increase in seismic velocities. This increase in velocity can be explained by the fact that gas hydrates are solids which occur in the pore space of the sediment. By increasing the amount of hydrates in the pore space the porosity itself drops which leads to an increase in the elastic moduli of the solid frame

(Dvorkin, 2004). Intuitively one would expect a reduction in attenuation with a stiffer rock matrix. However, it has been observed (Guerin and Goldberg, 2002, Wood, 2000, and Pratt et al., 2003) that with an increase in hydrate saturation the attenuation increased as well. A similar observation has been reported for ice (Prasad and Dvorkin, 2004). One possible reason for this behavior might be due to an increase in elastic heterogeneity which encourages pore-fluid crossflow between stiff and soft areas in the rock, triggered by the passing wave (Dvorkin, 2004).

The purpose of our experiments was to ascertain how much of the attenuation is caused by the hydrate itself. For that reason we performed ultrasonic velocity measurements on pure tetrahydrofuran (THF) hydrates. THF was chosen because of its stoichiometric relationship with water. By mixing 19 wt% of THF with 81 wt% of water the mixture should result in a 100 % pure THF hydrate. Also, the THF hydrate stability temperature is above the freezing point of water, meaning that if there is residual, unreacted water in the system, it is in a liquid phase.

Previous work focused on elastic effects of water-hydrates as well as elastic and anelastic effects in natural hydrate systems (sand+water+hydrate). No studies on hydrate - water systems. To explain the observed attenuations in natural hydrate systems (Guerin and Goldberg, 2002), we need to distinguish between attenuation due to the end members (sand and hydrates) from the attenuation arising from the interactions between the components. While attenuation in sands has been studied (Wang and Santamaria, 2007 and Liu et al., 2001), the intrinsic attenuation in ice and in hydrates has been largely ignored. Understanding attenuations in hydrate-bearing sediments is important to distinguish between seismic - blanking caused by reverberations as opposed to poor amplitude and frequency content due to attenuation.

Experimental Setup & Procedure

We used the ultrasonic pulse transmission technique and nuclear magnetic resonance (NMR) to study and characterize our samples.

To perform repeatable and reliable experiments, we designed a sample holder that allowed us to measure ultrasonic velocities of fluids (Figure 1). The sample holder consists of a tygon tubing sealed on each end with PEEK end caps. The end caps contained piezoelectric crystals (nominal frequency = 500 kHz) to generate and record acoustic waves as well as fluid lines for fluid injection. Small holes in the Tygon tubing held wires to position the PEEK end caps at a distance of 2 cm from one another. Finally, the sample holder was covered by softepoxy to prevent leakage of the fluid through the holes with the wires.

Sample Preparation Procedure:

We first prepared a de-aired stochiometric mixture of 19 wt% of THF and 81 wt% of water to ensure 100% THF hydrate formation. After the water-THF mixture was injected into the sample holder, the fluid lines were closed and the sample was submersed in a temperature controlled cooling bath. Ultrasonic p- and s-waves were recorded at room temperature (25° C) as well as at 1 °C and -10 °C. These temperatures were chosen to guarantee that THF-water mixture was at its liquid stage (25 °C) and at a temperature that is suitable for hydrate formation and stability (1 °C). As described earlier the hydrate stability temperature is above the freezing point of water. To verify that we achieved a 100 % conversion, we lowered the temperature to -10 °C which would allow residual water to freeze. Also, all of these measurements were conducted at atmospheric pressure.

We repeated our experiments three times. The first set was designed to capture changes in acoustic signals as a function of temperature. Thus, acoustic waveforms were acquired at 1 °C temperature steps. Since the waveforms and velocities only changed at specific temperatures, the second and third set of measurements were made at three temperatures (25°C; -1°C; and -10°C).

Acoustic Analysis:

At discrete temperatures, we collected waveforms to calculate ultrasonic velocities and frequency content. The travel times were measured by picking the first arrival of the signals after system delay

4

time and temperature corrections. The first cycle of the p-wave was also analyzed for its frequency content using a fast fourier transform. Ultrasonic attenuation was calculated by dividing the amplitude spectrum measured for a standard by the amplitude spectrum measured for the sample (Toksöz et al in 1978). The standard used in this study was aluminum. It assumes that the geometry and measuring procedure of the measured samples and the reference sample is the same. After dividing the frequency spectra, the slope of the resulting ratio is related to the quality factor Q (also known as attenuation).

$$Q = \frac{\pi * l}{\gamma * v} \tag{1}$$

Where Q is the quality factor, l the length of the samples [m], γ the slope of the frequency ratios [sec], and v the measured velocity [m/s]. We used an aluminum standard to benchmark our ultrasonic setup; to calibrate the delay times and for attenuation calculations.

Results

Acoustic Velocities:

Figure 2 shows the raw waveforms at various stages of hydrate formation. The measured velocities at each stage are shown in Table 1. Thus, the waveforms for the sample containing only the THF-water mixture were taken at room temperature; "100 %" hydrate at 1 °C, and hydrate and ice at -10 °C. It is noticeable that the compressional velocity increased by a factor of 2 in hydrate compared to the water. Also the peak-to-peak amplitude dropped. Further sample cooling to -10 °C resulted in another velocity increase as well as an increase in the peak-to-peak amplitude. Finally the waveform of the aluminium can be seen in Figure 2. The velocity calculation for its first arrival corresponds with literature values (Molotova et al, 1960). It is perceptible that the amplitude of the aluminum waveform is smaller than the one for the measured samples. This is due to the design of the used transducers. These transducers are designed to measure low velocity materials such as unconsolidated sands. The high impedance contrast between the PEEK end caps and the aluminum

causes parts of the signal to reflect of the aluminum instead of being transmitted through it. Additionally, Table 2 shows the wave numbers for a 2 cm long sample for the measured samples at various stages as well as for the aluminum.

Using the first cycles of the arriving wave and analyzing them regarding their frequency content is shown in Figure 3. It can be seen that the aluminum standard has much higher frequency content than the samples themselves, as expected. Furthermore, the frequency spectra are similar for all samples, showing that the measurements, especially for the hydrate bearing case, are reproducible. Similarly, the frequency spectra and the peak frequencies of the water samples and the frozen samples are also comparable (Figure 3 d). On the other hand the "pure" THF hydrate samples, yield lower peak frequencies as well as a much faster decay or a lesser amount of higher frequencies in the frequency spectrum.

Using equation 1, we calculated the p-wave attenuation (Figure 4). Low attenuation values were calculated for the liquid samples whereas an increase in attenuation can be observed after the hydrates form and this attenuation drops again to almost the same value as for the THF-water samples after the sample is cooled down to -10 °C.

Discussion:

The observed additional velocity increase in our ultrasonics data suggests that residual fluid in the sample converted into ice to cause an additional stiffening of the sample. Even though THF has a stoichiometric relationship with water, it is difficult to mix a mixture that results in 100 % THF hydrate. The one reason for that is that THF is extremely volatile and during the mixing process with water, some of the THF evaporates and the remaining mixture produces a sample containing excess water after hydrate formation. Thus, the conversion may not be 100 % efficient.

The drop in the main frequency peak as well as loss in higher frequencies indicates that the attenuation of the propagating wave, and is likely the result of energy lost as residual fluid between THF hydrate grains squirts through the intergranular spaces in response to wave-induced sample deformations (Johnston et al, 1979). However, after cooling the sample further, the residual water turns into ice and the attenuation drops nearly to that measured through liquid water. The fact that the frequency spectra for water and for THF hydrate with frozen residual fluid are so similar suggests there is little to no intrinsic attenuation within the THF hydrate phase itself. This implies that the residual fluid is now in a solid stage resulting in a lower attenuation.

Residual Fluid Identification:

As discussed in the previous section, all of our observations, the additional increase in velocity and drop frequency content as well as the drop in attenuation after the samples were cooled to -10 °C, indicate that there was residual fluid present in our hydrate samples. To identify the fluid that is left in the samples we performed nuclear magnetic resonance (NMR) measurements. NMR measurements are sensitive to free hydrogen atoms as they occur in liquid water or in liquid THF. In our study, we used a low-field (2 MHz) NMR device and a non negative linear spline to calculate T_2 relaxation times from exponential decay.

Three possible scenarios could be present in our experiments for the samples at 1 °C which were supposed to be 100 % THF hydrate. First, the mixture contained too much water resulting in a sample with only residual water after forming hydrates. Second, the mixture contained too much THF resulting in a sample with residual THF after forming hydrates. Or, while forming hydrates some of the water and THF gets separated, resulting in small pockets of water and THF which stay unreacted.

We prepared small glass vials with a THF-water mixture from the same batch that we used for the third set of acoustic measurements. These glass vials were submerged into the same cooling bath as

the sample holder for the ultrasonic measurements and measured at the same temperature stages. Again, all measurements were performed at atmospheric pressures. Figure 5a shows the raw data for T_2 relaxation for a sample that was measured in the NMR apparatus. The temperature at which it was measured was around 1 °C meaning that it is well below the hydrate stability temperature (~ 4°C) and above the freezing point of water. If the conversion from THF and water into THF hydrates would have been perfect, no signal should be observable. As we can see in Figure 5a, we have a small amplitude that relaxes fast indicating the presence of hydrogen, either in form of water or THF. The fast relaxation time indicates that this liquid is probably trapped between the hydrate crystals. The inversion (Figure 5b) of this measurement does not show a distinct peak and therefore it is impossible to quantify which of the two liquids is present in the sample. In Figure 5a we can also observe how the signal changes for the same sample after the hydrates start to dissociate. 62 minutes elapsed between the first and the last measurement. After 42 minutes (13th measurement) the T_2 relaxation does not change much indicating the complete dissociation of the hydrates. The acoustic signals (Figure 5c) show the corresponding first arrivals for the first and 13th measurement of the NMR. It can be observed that the velocity dropped whereas the inversion as well as the raw data amplitude of the NMR increased.

We performed the same NMR measurements with the sample being frozen (~ -10 °C). Figure 6 shows the raw data for the NMR measurement. As it can be seen, no signal is present in the data which leads to the conclusion that no residual fluid is present in the sample. This also means that the fluid that can be detected in the samples at 1 °C can only be free water. This is because the freezing point of THF is below -100 °C (Jones et. al, 2010).

Conclusions

In summary, using ultrasonic velocity and NMR measurements, we have shown that water, THF hydrate with residual water, and THF hydrate with frozen residual water are distinguishable by their acoustic attenuation and NMR signatures.

- THF Hydrate has an almost negligible attenuation

- Small amounts of residual water in the hydrate sample caused an significant attenuation

- A combination of NMR and ultrasonic measurements allows us to characterize gas hydrate formation as well as dissociation processes.

References

Dvorkin, J, R. Uden (2004), "Seismic wave attenuation in a methane hydrate reservoir" The Leading Edge Interpreter's Corner

Guerin, G., and Goldberg, D., (2002). Sonic waveform attenuation in gas hydrate–bearing sediments from the Mallik 2L-38 research well, MacKenzie Delta, Canada. J. Geophys. Res., 107:2088. doi:10.1029/2001JB000556

Johnston, D.H. ,M. N. Toksöz, and A. Timur (1979), Attenuation of seismic waves in dry and saturated rocks: II Mechanisms, Geophysics, 44, 691,

Jones, C. Y., J.S. Zhang, and J.W. Lee (2010), Isotope Effect on Eutectic and Hydrate Melting Temperatures in the Water-THF System, Journal of Thermodynamics, Volume 2010 (2010), Article ID 583041

Liu, Z., Rector, J. W., Nihei, K. T., Tomutsa, L., Myer, L. R., & Nakagawa, S. (2001). Extensional wave attenuation and velocity in partially-saturated sand in the sonic frequency range. Rock Mechanics in the National Interest. The Netherlands: Swets & Zeitlinger Lisse. - Report Number: LBNL-50831

Molotova and Vassil'ev (1960), Bull. (Izvest.) Acad. Sei. USSR, Geoph. Ser. (Eng. Ed.) 8, 731

Prasad, M., and J. Dvorkin (2004), Velocity and attenuation of compressional waves in brines, SEG Expanded Abstr., 23, 1666, doi:10.1190/1.1845150.

Pratt, R.,K. Bauer, and M. Weber (2003), Crosshole waveform tomography velocity and attenuation images of arctic gas hydrates, paper presented at 73rd Annual Meeting, Soc. Of Explor. Geophys., Dallas, Tex.

Sloan, E. D. & Koh, C. A. (2008), Clathrate Hydrates of Natural Gases. 3rd ed., CRC Press, Taylor & Francis Group, Boca Raton, FL

Toksöz, M.N., Johnston, D.H., and Timur, A., (1978), Attenuation of seismic waves in dry and saturated rocks: 1. Laboratory measurement; Geophysics, 44, 681-690.

Wang, Y.-H. and J.C. Santamarina, (2007), Attenuation in sand: an exploratory study on the small-strain behavior and the influence of moisture condensation, Granular Matter, Volume 9, Issue 6, pp 365-376

Wood, W.T., Holbrook, W.S. & Hoskins, H., (2000), "In situ measurements of P-wave attenuation in methane hydrate and gas bearing sediments on the Blake Ridge" Proc. ODP. Results, Vol 164, pp. 265-272, eds Paull, C., Matsumoto, R., Wallace, P. & others, Ocean Drilling Program, College Station, Texas

Table 1: Summary of calculated velocities, peak frequencies, and peak-to-peak amplitudes for all the samples.

(PT = pressure and temperature)

Condition / Property	THF+DI-Water Ambient laboratory PT	Hydrate -1 °C	Frozen -10 °C	Aluminum Ambient
Compressional Velocity (m/s)	1550 ± 11 (Avg. of 18 measurements)	3150 ± 95 (Avg. of 20 measurements)	3560 ± 63 (Avg. of 12 measurements)	6030
Average Peak Frequency [kHz]	266.1 258.6 304.4 } 276.3	197.1 183.6 180.9 } 187.2	246.6 245.2 } 245,9	335.2
Peak to Peak Amplitude (V)	2.176 2.0402 2.2228 } 2.1463	0.9944 1.1097 0.9110 } 1.0050	1.7 1.6978 } 1.69	0.46
Slope of the Frequency Ratios α	5.63 e^6 5.81 e^6 4.66 e^6 } 5.36e^6	9.71 e^6 9.85 e^6 9.2 e^6 } 9.35e^6	3.43 e^6 3.24 e^6 } 3.335e^6	
Attenuation Q	7.5699 7.3354 9.1456 } 8.02	2.1549 2.1243 2.2744 } 2.18	5.3983 5.7149 } 5.556	

Table 2: Estimated wavelengths for various sample types with their corresponding wavelength numbers in a 2 cm long sample.

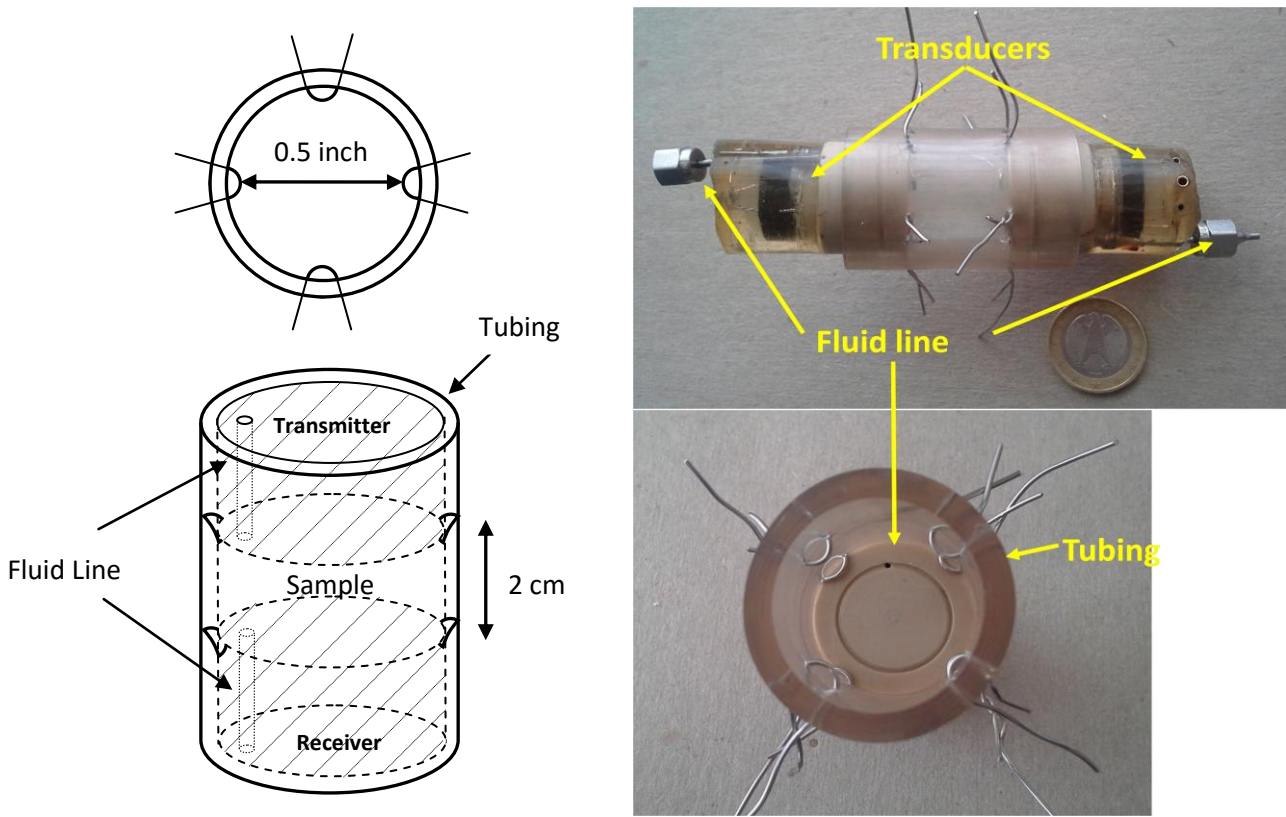| State	$\lambda = \dfrac{v}{f} \quad \left[m = \dfrac{\frac{m}{s}}{\frac{1}{s}} \right]$	Number of wavelengths in a sample with a length of 2cm
THF+DI-Water	$\dfrac{1550}{5000000} = 0.31\ cm$	≈ 6.7
Hydrate	$\dfrac{3150}{5000000} = 0.63\ cm$	≈ 3.3
Frozen	$\dfrac{3560}{5000000} = 0.712\ cm$	≈ 2.94
Aluminum	$\dfrac{6030}{5000000} = 1.206\ cm$	≈ 1.74

Figure 1: A) Schematic of the sample B) Photograph showing the transducer and receiver holders. The wires extending from sample are clipped before measurements and sealed with softepoxy. Tubing is sealed against transducer and receiver using a metal wire.
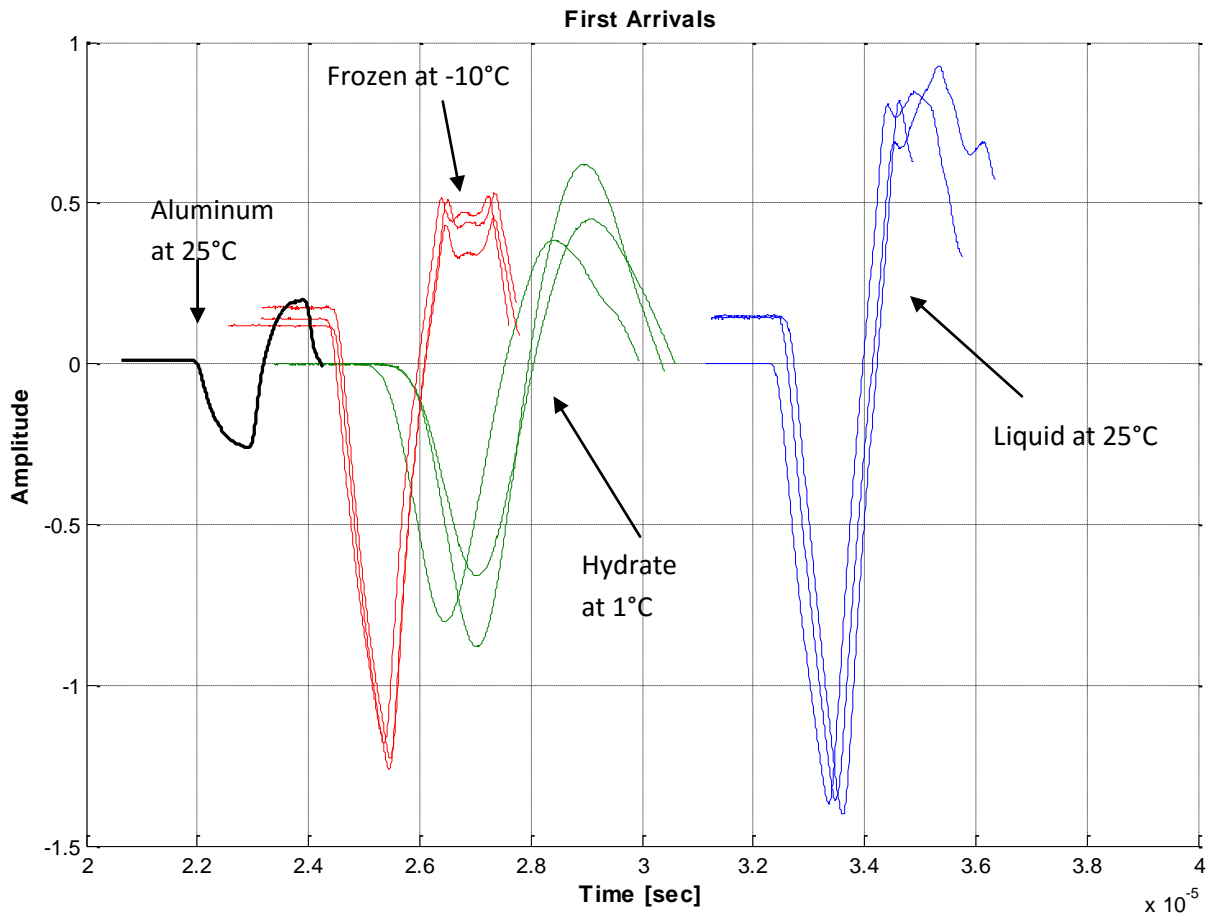
Figure 2: Raw waveforms for the first arrivals for the p-waves in aluminum standard (black), frozen sample (red), only hydrate bearing (green), and liquid (blue). Note that total travel time is through peek and sample. The aluminum and Liquid samples were measured at room temperature (25 °C), Hydrate samples at 1 °C and frozen samples at -10 °C. All measurements were conducted at atmospheric pressure. Multiple lines at the same conditions mark repeat measurements.
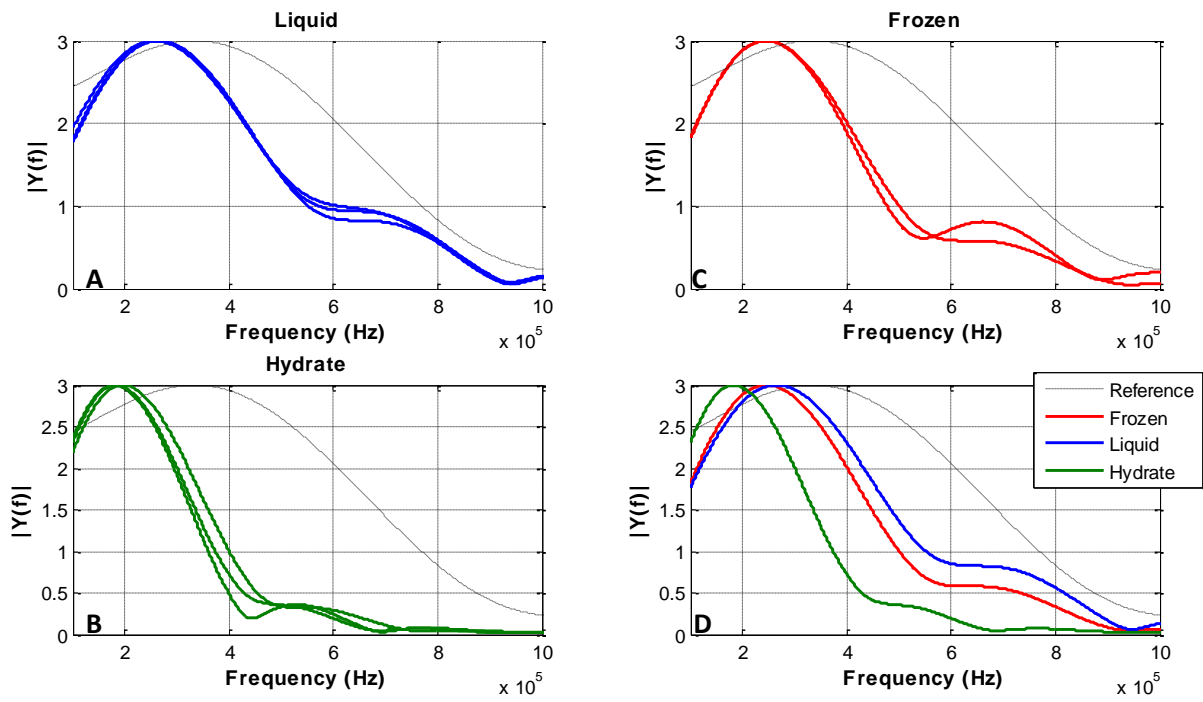
Figure 3: Frequency spectra of waveforms shown in Figure 2 for different samples. A) THF-Water B) "100 %" THF hydrate sample C) frozen sample D) Comparison of Liquid, Hydrate, and Frozen frequencies. Time progression of the experiments were day 0 = Liquid data, day 3 = Hydrate data, and day 4 = Frozen data.
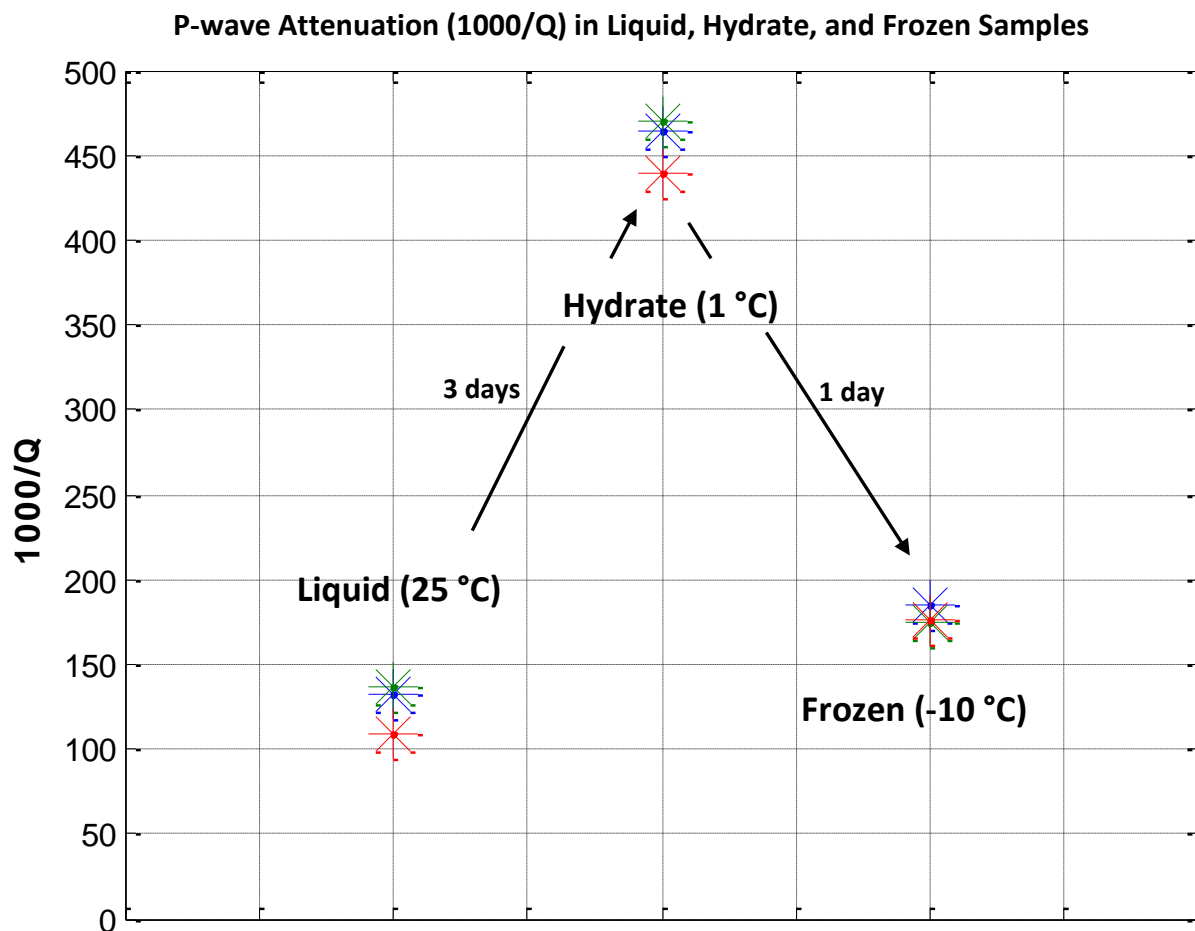
Figure 4: Overview of the calculated attenuation Q for the liquid, hydrate and frozen samples. Lines denote successive formation of the samples as well as their temperatures at measurements. The different symbols mark separate measurements.
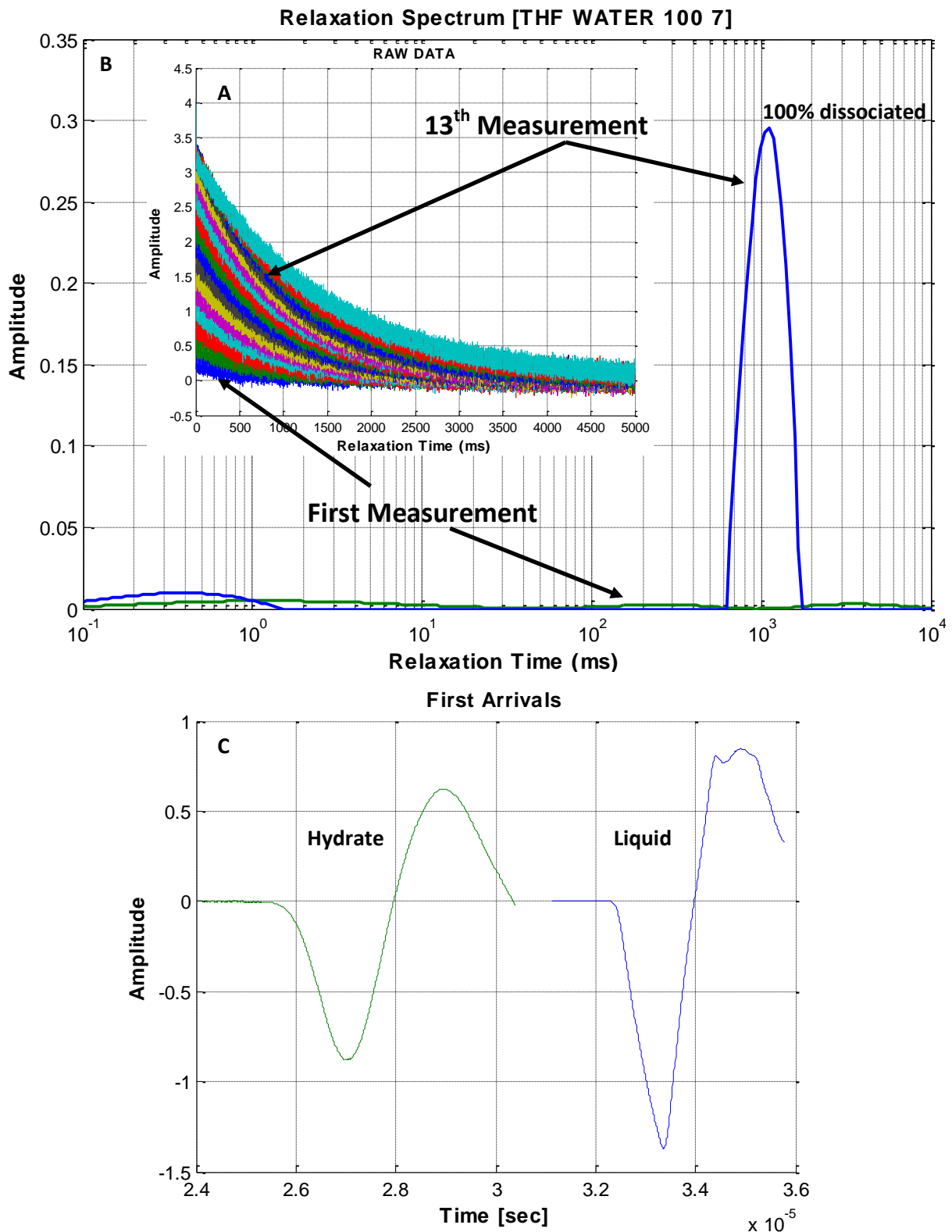
Figure 5: A) Raw data for a sample containing "100 %" THF hydrate. Continuous measurements show an increase in amplitude and longer relaxation times which are a result of the dissociation of the hydrate and therefore the availability of more free hydrogen. B) Inversion of a sample containing "100 %" THF hydrate. Comparison of the First Run at 1 °C with a measurement performed after hydrates were completely dissolved. Inverted signals below an amplitude of 0.01 should not be considered since they may result from inversion artifacts. C) First arrivals for the sample containing only hydrates (green) which corresponds to the first measurement of the NMR and the first arrival of the sample in the liquid stage (blue) which corresponds to the 13th measurement of the NMR.
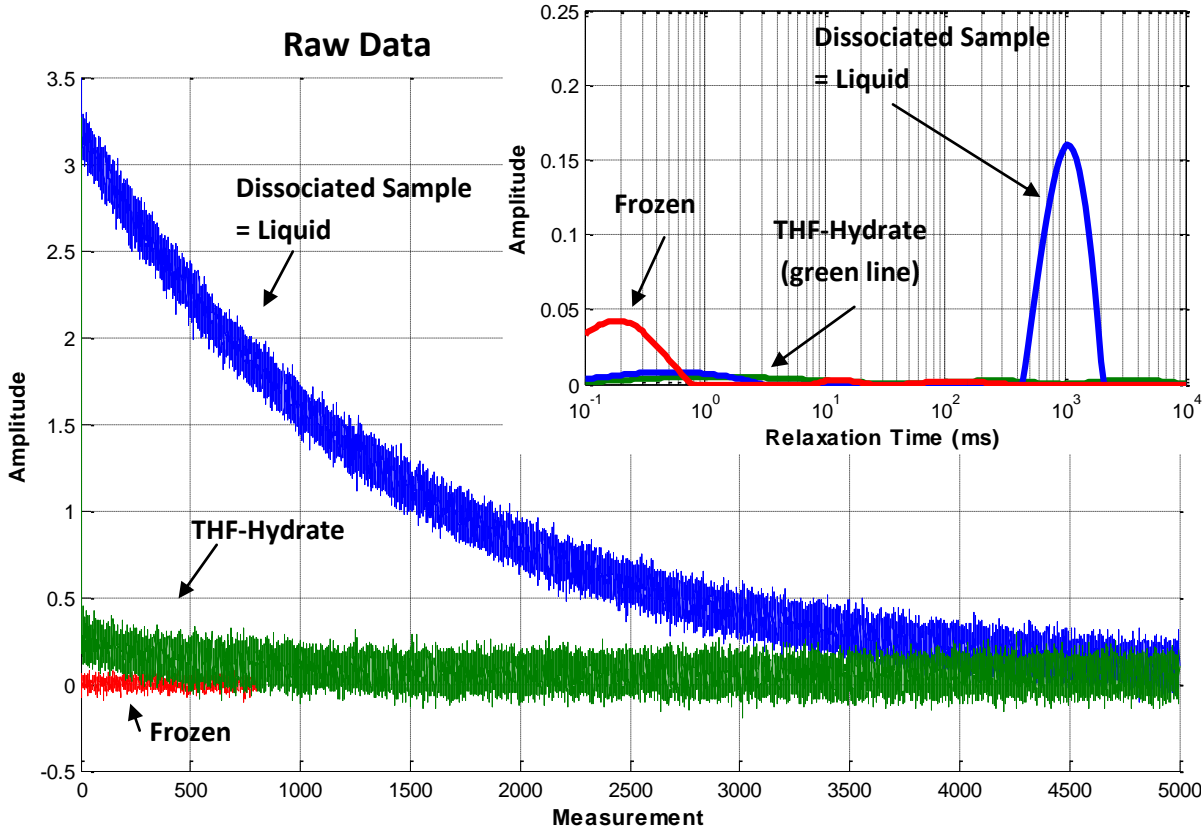
Figure 6: Relaxation Time for the First Run of a sample containing "100%" THF Hydrate at -10 °C. Note: subtle difference in relaxation spectra of Frozen and Hydrate sample. To resolve these differences, controlled pressure and temperature conditions with fast relaxation sensitivity equipment are needed.

Micro X-Ray Computed Tomography Imaging and Ultrasonic Velocity Measurements of Hydrate-Bearing Sediments

Mandy Schindler[*], **Michael L. Batzle**[†] **and Manika Prasad**[*]

[*]*Colorado School of Mines,*

1500 Illinois Street,

Golden, CO, 80401

manschin@mines.edu

[†] *Deceased*

ABSTRACT

Naturally occurring gas hydrates contain significant amounts of natural gas which might be produced in the foreseeable future. Thus, it is necessary to understand the pore-space characteristics of hydrate reservoirs, especially the pore-scale distribution of hydrate and its interaction with the sediment. There are four different models for hydrate distribution in the pore space: pore filling, sediment-frame component, envelope cementing and contact cementing. The goal of this study is to compare the models with pore scale hydrate distribution in laboratory formed hydrates and its effects on seismic velocities and sonic logs. Our results can be used to estimate hydrate saturation from seismic velocities and sonic logs.

1

Laboratory measurements were conducted. Tetrahydrofuran (THF) was used as a guest molecule since THF hydrate is a proxy for naturally occurring hydrate. We performed micro X-ray computed tomography (MXCT) to obtain information about the distribution of hydrate in the pore space of synthetic sediment (glass beads). We also made ultrasonic velocity measurements on the same samples. Both, MXCT images and ultrasonic velocity measurements, indicate that THF hydrate forms in the pore space with only a small portion contacting the grain surfaces. A small part of the hydrate appears to bridge and support the sediment grains. These hydrate-bearing sediments appear to follow a pore-filling model with a small part of the hydrate becoming part of the sediment frame. Based on this knowledge, it may be possible to calibrate seismic and well logging data to calculate the amount of natural gas stored in a hydrate reservoir.

LIST OF FIGURES

4

LIST OF TABLES

INTRODUCTION

Gas hydrates are clathrate structures of natural gases. They require low temperatures and high pressures for stability. The widespread occurence of gas hydrates in permafrost and shallow marine sediments along continental slopes is well established (Collett *et al.*, 2009). The estimated amount of natural gas, mainly methane, stored in hydrate reservoirs exceeds the amount of natural gas stored in conventional resources by at least one order of magnitude (Meyer, 1981; Dobrynin *et al.*, 1981; Collett *et al.*, 2009). Anderson *et al.* (2008) and Dallimore *et al.* (2008) demonstrated that gas-hydrate production can be developed with existing oil and gas production technology. Before successful production of methane gas from hydrate reservoirs we need to attain knowledge about physical properties of gas-hydrate bearing sediments.

The most common geophysical methods used to characterize and quantify gas hydrates in nature are seismic surveying and well logging. In order to calibrate and interpret these field measurements, laboratory studies are necessary to determine the bulk physical properties of hydrate-bearing sediment. Currently, it is possible to predict the existence of gas hydrates from geophysical measurements. However, the techniques used to estimate hydrate saturation based on either seismic data or well logs require further development (Collett and Lee, 2012). The amount of gas hydrate stored in a reservoir remains uncertain because the relationship between saturation and seismic or sonic velocities depends largely on the pore-scale distribution of gas hydrate. The models described by Ecker *et al.* (1998) and Helgerud *et al.* (1999) show that a very small amount of cementing gas hydrate presents itself with similar velocities as a high saturation of pore-filling gas hydrate. Thus, information about the distribution of gas hydrates in the rock is necessary to determine hydrate saturation. It

6

is imperative to ascertain hydrate-sediment interactions in addition to physical properties of pure hydrate (Yun *et al.*, 2005).

In this study, we focus on the pore-scale distribution of gas hydrates in synthetic coarse-grained porous media with high permeability. Coarse grained sand reservoirs, as they exist in permafrost regions and marine environments, are relatively easy to access and thus more likely to permit methane production from gas hydrates than hydrate reservoirs in shale (Boswell and Collett, 2006). Gas hydrates occur as massive units and lenses in fractures of fine-grained material (shale) as well as distributed in the pore space of coarse-grained porous media (Figure 1).

Hydrate distribution in the pore space depends mainly on the formation method. In nature, gas hydrates are formed in two ways: (1) from methane dissolved in water or (2) from free methane gas (Collett *et al.*, 2009). Hydrate formed from methane gas tends to form at the grain surface and grain contacts (Waite *et al.*, 2004; Priest *et al.*, 2005) while hydrate formed from methane dissolved in water tends to form in the pore body with little or no contact to the sediment grains (Ecker *et al.*, 1998; Kunerth *et al.*, 2001). These conclusions are based on the velocities matching effective medium models, however, to date there is little direct verification for the pore-scale distribution. Very limited research has been done on imaging the hydrate distribution in the pore space (e.g. Kerkar *et al.* (2009), Kerkar *et al.* (2014), Chaouachi *et al.* (2015)). Our study provides imaging of the pore-space distribution of hydrate and velocities in addition to the images thus providing a link between the effective medium models and direct visual observations of hydrate in the pore space.

Gas hydrate in coarse grained, marine sediments is more likely to form from methane

dissolved in water, whereas gas hydrate in permafrost regions is associated with formation from free methane gas (Collett *et al.*, 2009). Our goal is to determine the pore-scale distribution of hydrate formed from gas dissolved in water and the corresponding acoustic velocities . As a proxy for this formation mechanism we used tetrahydrofuran (THF) as a guest molecule. We use micro X-ray computed tomography (MXCT) images to image hydrate distribution in the pore space. In addition, we investigated the influence of hydrate saturation and distribution on ultrasonic velocities. The relation between pore-scale distribution, hydrate formation method and acoustic velocities is essential to determine the amount of hydrate in a reservoir from seismic data and sonic logs.

Effective Medium Modeling

Seismic and acoustic velocities are influenced by changes in hydrate saturation. However, in addition to hydrate saturation velocities will behave differently for different hydrate distributions in the pore space. Theoretical models infer different pore-scale hydrate distributions and their impact on acoustic velocities. One such model is the effective medium theory applied to hydrate-bearing sediments by Ecker *et al.* (1998) and Helgerud *et al.* (1999).

Figure 1 shows four different pore-scale distributions according to this effective medium model for gas hydrates in sediment: contact cementing, envelope cementing, pore filling and sediment frame component. The contact-cementing hydrate causes a drastic increase in ultrasonic velocities even for small amounts of hydrate present in the pore space whereas hydrate formed according to the pore-filling model shows a much smaller influence on the ultrasonic velocities. Hydrate formation from free gas appears to create grain-cementing
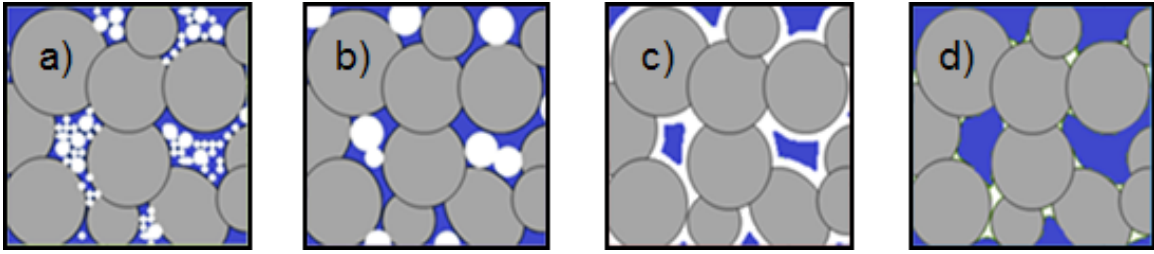
Figure 1: Conceptual images of possible hydrate distributions in the pore space. Gray spheres represent sediment grains, pore fluid (e.g. brine) is shown in blue and hydrate in white. a) pore filling hydrate b) frame-component hydrate c) envelope-cementing hydrate d)contact-cementing hydrate. Figures modified from Rydzy and Batzle (2011)

hydrate, which resembles the contact or envelope-cementing models (Waite *et al.*, 2004; Priest *et al.*, 2005). Hydrate formed from gas dissolved in water seems to have little or no contact with the sediment grains and thus conforms to the frame-component or pore-filling model (Kerkar *et al.*, 2014). Laboratory measurements are necessary to determine the correlation of hydrate distribution in the pore space with ultrasonic velocities and to corroborate previous results.

MATERIALS AND METHOD

We utilized ultrasonic velocity measurements and micro X-ray computed tomography (MXCT). MXCT was used for direct visual observation of hydrate distribution in the pore space. Ultrasonic velocity measurements were used to show how the velocities change for different hydrate saturations. The combination of these two measurements can be compared to effective medium models. The materials in the sample were borosilicate glass beads as host

sediment, THF as guest molecule and methane proxy, DI water and barium chloride to obtain a density contrast between THF hydrate and residual brine.

Proxy for Natural Gas Hydrate

The most common hydrate in nature is methane (CH_4) hydrate. Methane hydrates either need to be cooled to -78.7 °C to be stable under atmospheric pressure (Sloan and Koh, 2008) or require a pressure of 4 MPa to be stable at 4 °C (Carroll, 2009). The controlled synthesis of methane hydrate from the aqueous phase is additionally difficult, mainly because of the low solubility of methane in water ($1.5 \cdot 10^{-3}$ mol methane per 1 mol water at 5 MPa and 25 °C (Lide and Frederikse, 1995). This low solubility necessitates extensive pore fluid circulation and long experimental time for hydrate formation from the aqueous phase (Spangenberg *et al.*, 2005).

We used THF which forms hydrates at atmospheric pressure and temperatures of 4 °C (Sloan and Koh, 2008). THF is a heterocyclic ether with the molecular formula C_4H_8O. THF is completely miscible in water (Sloan and Koh, 2008) and thus widely used to resemble hydrate formation from methane dissolved in water (Pearson *et al.*, 1986; Collett and Ladd, 2000; Yun *et al.*, 2005). Lee *et al.* (2007) demonstrated that THF and methane hydrates exhibit similar macroscale mechanical, electrical and thermal characteristics. THF has the advantage of providing close control on the hydrate saturation by varying the stoichiometric THF-H_2O mixture without having the long formation history of methane hydrate. However, it should be noted that THF hydrate forms structure-II hydrates whereas pure methane forms structure-I hydrates. Hydrates in nature, especially when formed from thermogenic gas, often contain longer chain hydrocarbons (e.g. ethane, propane) in addition to methane

and thus can form structure-II hydrates (Sloan and Koh, 2008) . Therefore, THF hydrate is used as a proxy for naturally occurring gas hydrate.

Sample Composition and Preparation

Sample components were unconsolidated borosilicate glass beads (diameter: 1 mm) used as host sediment, de-ionized water, THF and barium chloride. In contrast to sediment grains, glass beads have a uniform X-ray attenuation value, shape and density ($2.23 \, \text{g/cm}^3$) allowing for easier interpretation of the MXCT images. We used barium chloride as a CT contrast agent and a proxy for naturally occuring sodium chloride brine. Stoichiometric mixtures of THF and water were used to obtain different hydrate saturations. The specimen exhibited a porosity of approximately 0.35. The porosity was determined from CT images.

The same sample composition was used for ultrasonic velocity measurements and MXCT imaging. For the MXCT samples, the liquid mixture of THF, barium chloride and DI-water was added to the dry borosilicate glass beads through a syringe. MXCT samples were formed directly in the pressure vessel and had a diameter of 7 mm and a length of 80 mm. For the ultrasonic samples, a sleeve of heat-shrink tubing was placed between two ultrasonic transducers, filled with borosilicate glass beads and then evacuated before the mixture of THF, water and barium chloride was injected with a pore pressure of 0.3 MPa. The sample size of the ultrasonic samples was 20 mm diameter and 25 mm length.

Table 1 shows all samples which have been measured. MXCT imaging was performed on four samples, two with 40% hydrate saturation and two with 80% hydrate saturation. We chose to measure two samples of each saturation to verify repeatability of the experiment. Ultrasonic velocity measurements were obtained for 5 samples with saturations of 40%,

Table 1: List of measured samples

S_h	Ultrasonic	MXCT
40%	2	1
60%	0	2
80%	2	1
100%	0	1

60%, 80% and 100% and one additional sample with 60% hydrate saturation which did not

contain barium chloride. These saturations were chosen in order to compare the measured

ultrasonic velocities with the effective medium models.

Micro X-Ray Computed Tomography

MXCT imaging was performed in the MicroXCT-400 apparatus from XRadia. A Torlon

(poliamide-imide) pressure cell with stainless steel fittings on both ends was used. The

pressure cell has an inner diameter of 7 mm and a length of 80 mm (Figure 2). The setup

was temperature controlled by cooled air. Air from a compressor is transported through

a copper-coil located in a cooling bath ($T_{bath} = -30°C$)and then led through a thermally

insulated hose into the CT apparatus. The insulated section between cooling bath and CT

apparatus also contains a hose loop which circulates cooled ethylene glycole alongside the

air hose for additional cooling. This setup provides cooling for periods of multiple days to

keep the hydrate stable while high-resolution CT scans are performed. The temperatures
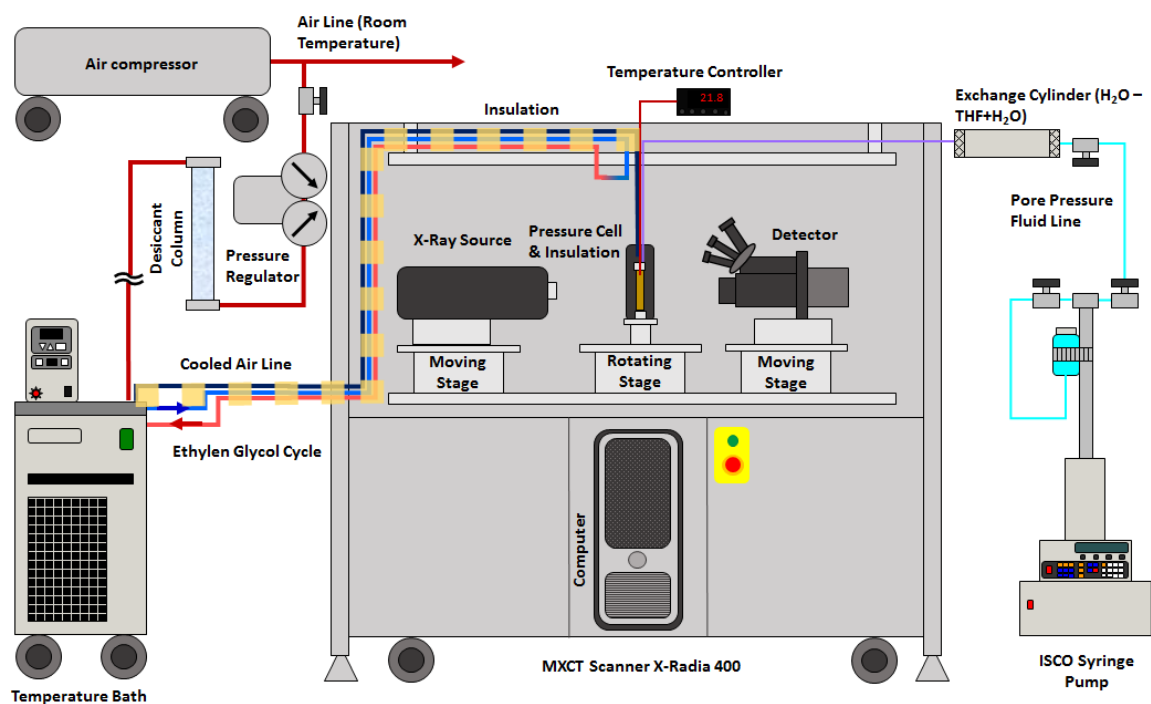
Figure 2: Experimental setup for MXCT imaging

were kept stable $1\pm 0.5°C$ for the duration of the imaging process. The temperature was constantly kept above 0 °C to avoid the formation of ice along with THF hydrate.

MXCT measurements allow the distinction between materials based on their X-ray attenuation. X-ray attenuation is proportional to a product of bulk density and effective atomic number of each material (Van Geet *et al.*, 2000). Thus, MXCT imaging provides insight into the distribution of different sample components in the pore space. The output data of the MXCT apparatus are gray scale images. Grey values are proportional to X-ray attenuation, which depends on bulk density and the effective atomic number of each sample component at the used X-ray energy. Dark gray areas indicate low attenuation, light gray to white areas correspond to high attenuation.

Barium chloride was added to the fluid mixture to enhance the density contrast between residual brine and hydrate. A higher density contrast leads to a contrast in X-ray attenuation and thus to distinguishable gray values in the images. As hydrates form, barium chloride is excluded from the hydrate structure and remains within the water phase. The bulk densities of each sample component are listed in Table 2. We used an initial salinity of 3.2% for the sample with 80% hydrate saturation and 8.3% for the sample with 40% resulting in a salinity of 12.3% in the residual brine for both samples after hydrate formation. The amount of barium chloride was adjusted for each sample in order to obtain a density of 1.1 g/cm^3 for the remaining water assuming that all THF in the sample has been converted to hydrate.

In this study, the hydrate-bearing sample was monitored after the hydrate-formation process was completed. MXCT imaging of THF-hydrate dissociation was discussed in Schindler and Batzle (2014). X-ray source voltage of 150 kV and power of 6.2 Watt were used for all tomographies. Magnification of 0.5X (resolution 14.9 μm and 45.4 μm) was used to obtain a big field of view and thus an overview over the sample, magnification of 4X (resolution 5 μm) was used for a detailed view of the pore space. Best results were obtained for angular increments of 0.1° to 0.2° resulting in scanning durations of 1.5 for 0.5X magnification to 6 hours for 4X magnification.

Ultrasonic Velocity Measurements

The basic principle behind pulse transmission ultrasonic velocity measurements is to send an acoustic signal through a sample and measure the signals travel time. Therefore transducers with piezoelectric PZT crystals for P- and S-wave are attached to a sample jacketed with

heat-shrink tubing. Figure 3 shows a schematic of the experimental setup. More detailed information about the experimental setup and methodology can be found in Schindler and Batzle (2014).

After the described sample preparation, the temperature was gradually decreased below hydrate stability temperature (4.3 °C for 100% THF hydrate saturation). Waveforms for compressional and shear waves were recorded during the cooling process for each 1 °C interval. At temperatures close to the hydrate stability zone, waveforms were recorded more frequently (approximately every 0.2 °C). The cooling process was continued until hydrate formed in the sample. After hydrate formation, the sample was cooled further until the remaining water in the pore space froze. The further cooling until ice formation was performed to rule out ice as the reason for the first observed velocity increase. Differential scanning calorimetry has shown that the addition of 5 wt% barium chloride decreases the dissociation temperature of ice to -7.9 °C and the hydrate equilibrium temperature to 3.8 °C. Thus, the samples had to be cooled below 0 ° to form ice.

First arrival times were picked from waveforms (Figure 4). The sample length was determined from MXCT images. Ultrasonic velocities can be determined from arrival time and sample length:

$$v = \frac{l}{t - t_0} \tag{1}$$

where l is the length of the sample, t is the first arrival time and t_0 is the dead time (the travel time of a pulse from one transducer assembly to the other without a sample in between).
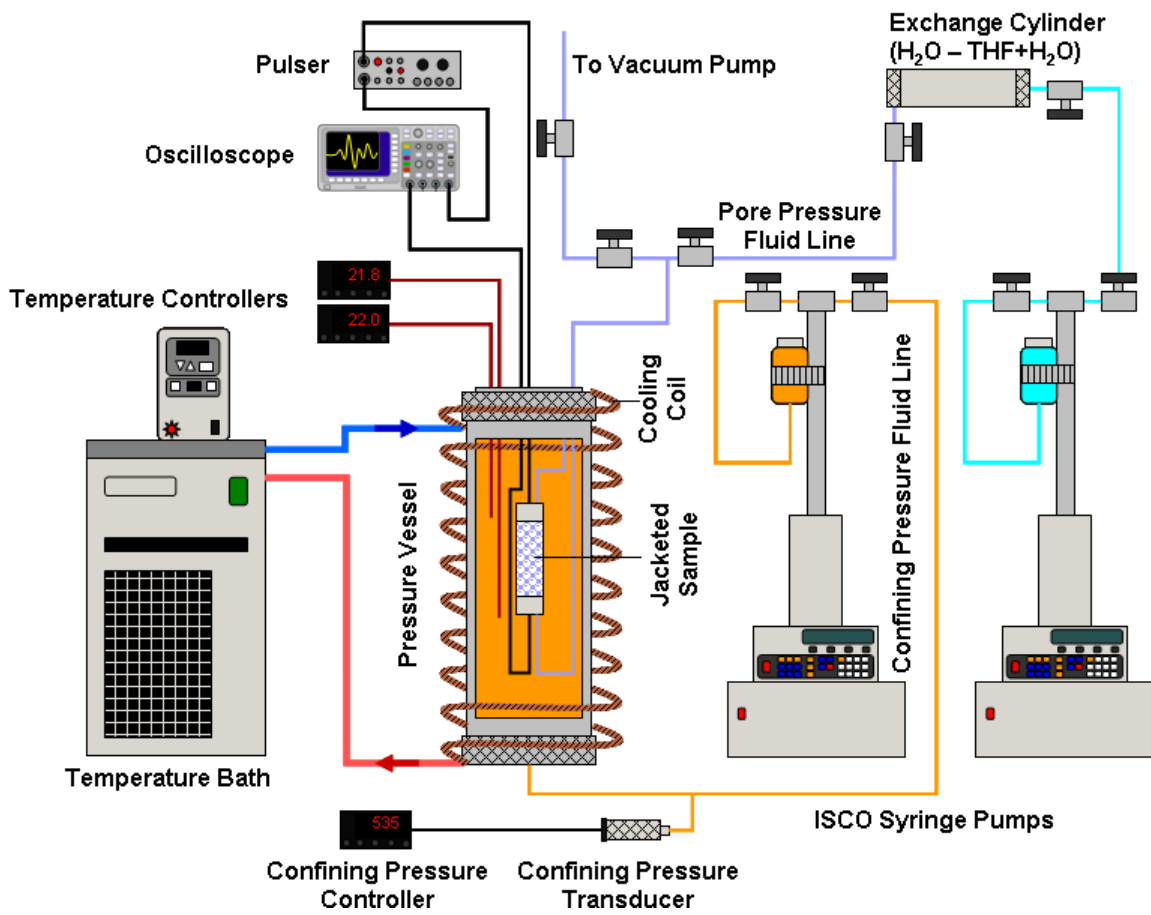
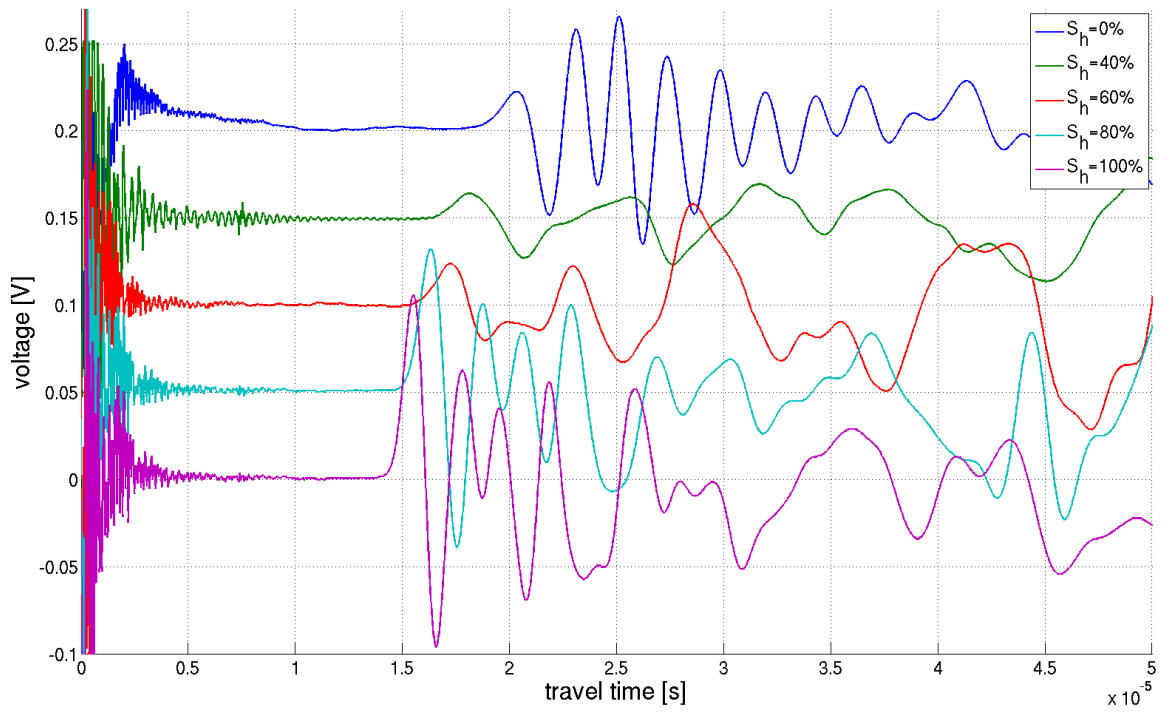Figure 3: Experimental setup for ultrasonic velocity measurements

Figure 4: Ultrasonic waveforms of samples with different hydrate saturations. A decrease in P-wave arrival times with increasing hydrate saturation was observed

RESULTS AND DISCUSSION

Micro X-Ray CT Imaging

The reconstructed CT images (Figure 5) contain information about the distribution of different components in the samples. Different gray values in the CT images represent different X-ray attenuation values in the sample. Because of its low attenuation (Table 2), THF hydrate has low gray-values and appears as violet and black areas in the CT images whereas barium chloride brine has higher gray values caused by its higher attenuation value (Table 2) and is displayed in yellow and white.

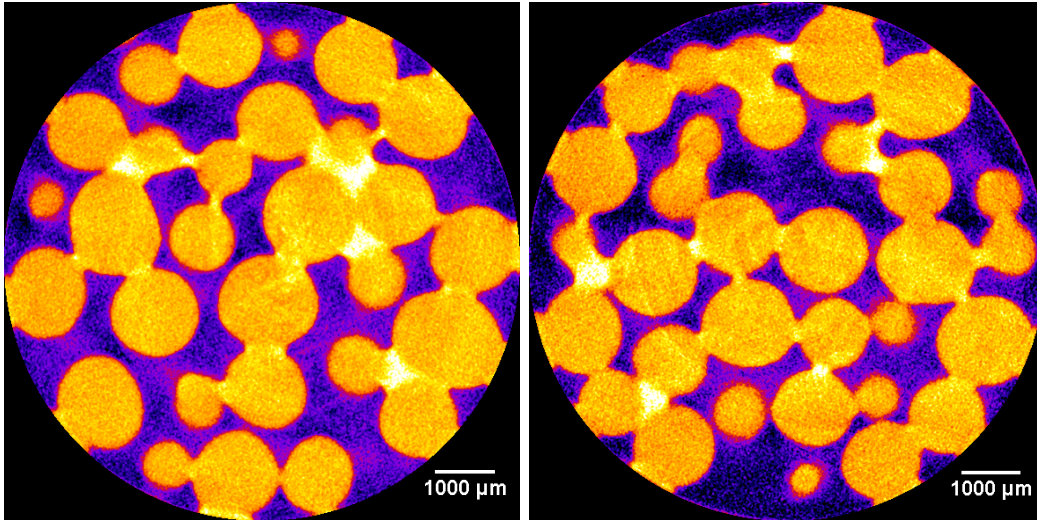
Figure 5: CT image showing horizontal slice through sample with S_h=40% (left) and S_h=80% (right). Resolution of 14.9 μm. White/light yellow: barium chloride brine, yellow/orange: glass beads, violet/black: THF hydrate

Figure 5 shows CT images for two samples with 40% and 80% hydrate saturation. The images indicate that THF hydrate is located in the pore body . However, it appears to

Table 2: Density of sample components included in MXCT samples. a) from Lide and Frederikse (1995), b) from Sloan and Koh (2008)

Component	Density [g/cm^3]
water	1.00
BaCl$_2$	3.84[a]
BaCl$_2$ brine (12.3 wt%)	1.1
THF hydrate	0.97[b]
THF-water-BaCl$_2$ mixture	1.00

touch the grain surfaces in a lot of areas indicating no clear conformity with any of the distribution models described by Ecker *et al.* (1998) and Helgerud *et al.* (1999). Barium chloride brine is found mainly at the grain contacts and fills some small pores entirely. THF hydrate is distributed evenly throughout the entire sample; heterogeneity was not observed. For image analysis, *ImageJ* was used. *

Ultrasonic Velocity Measurements

P and S-wave velocities were recorded for each sample during the cooling from 23 °C to -8 °C. Figure 6 shows the P-wave velocities recorded during cooling for all samples until hydrate formation was completed. Figure 7 shows P and S-wave velocities for the sample with 40% hydrate saturation including the entire cooling process until ice was formed. The

---

*ImageJ is a free image processing package mainly used for medical imaging. It is available at http://imagej.nih.gov/ij/

errors for P and S-wave velocities are about 5% and 20% to 23%, respectively (Table 3). Errors in velocity were calculated by propagating the uncertainties in sample length and picking of arrival times:

$$\sigma_v = v \cdot \sqrt{\sigma_l^2 \left(\frac{\partial v}{\partial l}\right)^2 + \sigma_t^2 \left(\frac{\partial v}{\partial t}\right)^2 + \sigma_{t_0}^2 \left(\frac{\partial v}{\partial t_0}\right)^2} \tag{2}$$

where v is the velocity, l is the length of the sample, t is the arrival time, t_0 is the dead time, σ_l is the uncertainty in sample length, σ_t is the uncertainty in arrival time, σ_{t_0} is the uncertainty in dead time, and σ_v is the absolute error in velocity.

The sample length was determined with MXCT in four different positions. Half of the difference between the longest and the shortest measured length was used as the error in sample length. The arrival time for the compressional wave is picked manually at the first significant divergence from zero in amplitude. Since the manual pick is subjective, an error of $\sigma_t = 10^{-7}s$ is assumed. The shear wave is picked at the first amplitude maximum since the first divergence from zero for the shear wave is not visible due to signal quality. This introduces an error of $\sigma_t = 5 \cdot 10^{-6}s$ resulting in a much larger error for the S-wave than for the P-wave. However, the arrival times were picked at the same location for each of the waveforms. Thus, the relative error is much smaller than the absolute error displayed in Figure 7 and Table 3. Our analysis concentrates on P-wave velocities because of the large error in S-wave velocities. An error of 5% is assumed for hydrate saturations. THF is highly volatile. Thus, a part of it can be lost during the sample preparation leading to lowered THF-hydrate saturations.

The equilibrium temperature for THF hydrates and water is 4.3 °C for 100% hydrate saturation. Hydrate formation started at temperatures below 4.3 °C. Reasons are the addi-

Figure 6: Ultrasonic P-wave velocities during the cooling of samples with different hydrate saturations. The THF-hydrate-water equilibrium temperature is shown for all used hydrate saturations. An increase in velocities indicates the presence of hydrate in the sample. Higher hydrate saturation resulted in higher P-wave velocities. Error bars are shown exemplary for one data row with 80% hydrate saturation. The formation of ice was decreased to about -8 °C due to the addition of barium chloride.
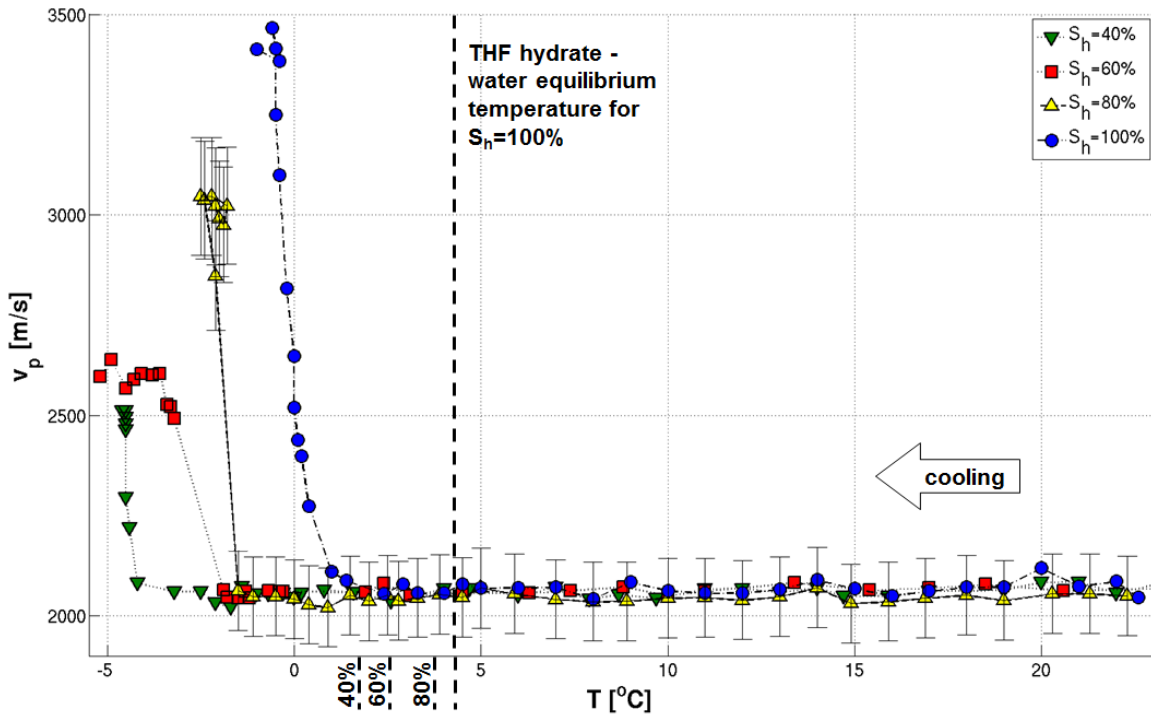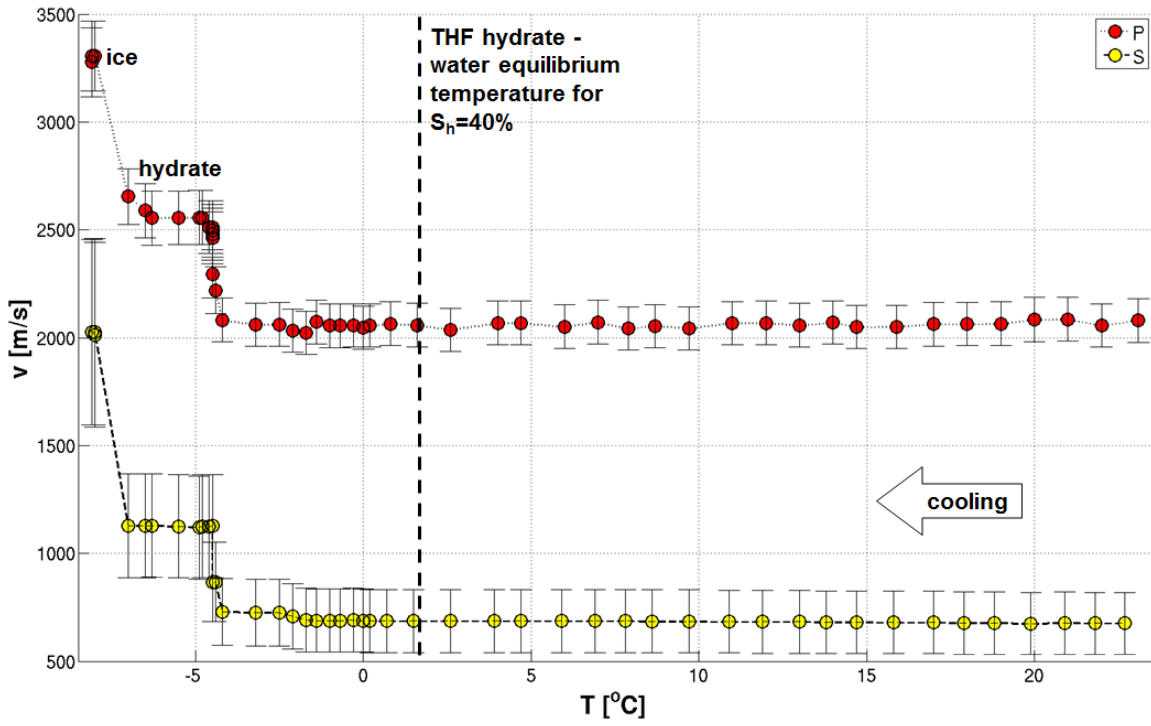
Figure 7: Ultrasonic P and S-wave velocities recorded during the cooling of a sample with 40% hydrate saturations. The THF-hydrate-water equilibrium boundary is shown for 40% hydrate saturation. After hydrate formation the sample was cooled further until the residual water froze resulting in a further velocity increase.

tion of barium chloride and the sub-cooling required to initiate hydrate formation (personal communication with E. D. Sloan). Furthermore, 4.3 °C is the equilibrium temperature for 100% hydrate saturation. For lower hydrate saturations, the equilibrium temperature decreases (Sloan and Koh, 2008) as shown in Figure 6. Additionally, the temperature was recorded in the confining fluid outside of the sample. Thus, it is assumed that the temperature of the sample was slightly higher than the measured temperatures. An increase in velocities which is attributed to the presence of hydrate in the pore space was first observed below 0 °C for all samples except the one with 100% hydrate saturation. A second increase in velocities indicated the formation of ice at lower temperatures of approximately -8 °C (Figure 7). Although the hydrate formation started at temperatures below 0 °C, the simultaneous formation of ice in the sample can be ruled out due to the second increase in velocities.

Figure 6 shows the P-wave velocities recorded during the cooling of four samples with four different hydrate saturations. The velocities remain approximately constant before hydrate stability temperature was reached. Hydrate stability temperature decreases with decreasing hydrate saturation (Makino *et al.*, 2005). The velocity increase is directly proportional to hydrate saturation: the more hydrate in the pore space, the higher the higher the velocity increase. A velocity increase became apparent at temperatures below the THF hydrate stability temperature. We are speculating that the hydrate formation started before we observed an increase in P- and S-wave velocities. Hydrate formed first in small amounts in the pore fluid which was not detected by the ultrasonic velocities. As the hydrate saturation approached higher numbers and hydrate started to touch the grains we see significant increases in velocities (Figures 6 and 7).

Figure 8 demonstrates how the measured ultrasonic velocities at different hydrate satu-

Table 3: Ultrasonic velocities after hydrate formation

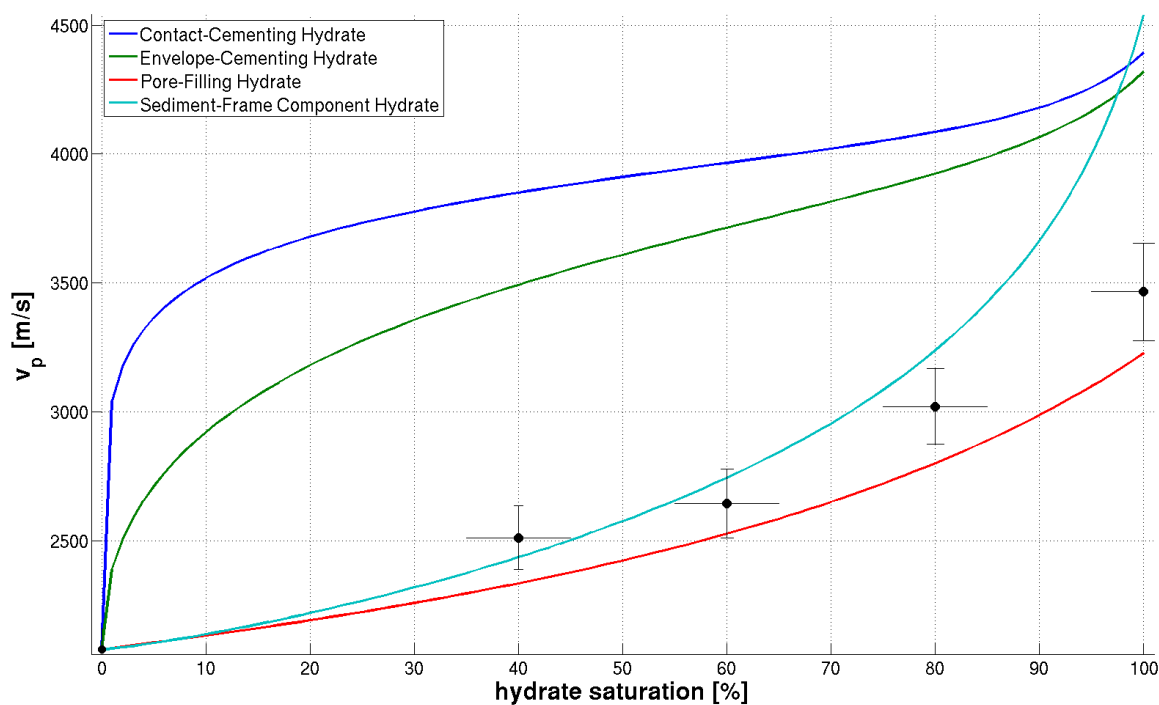| S_h [%]	v_p [m/s]	v_s [m/s]
0	2078 ± 83	658 ± 131
40 ± 5	2512 ± 123	1025 ± 218
60 ± 5	2645 ± 133	1057 ± 233
80 ± 5	3021 ± 146	1185 ± 255
100 ± 5	3466 ± 189	1187 ± 275

Figure 8: Effective medium model after Ecker *et al.* (1998) and Helgerud *et al.* (1999) with compressional wave velocities obtained by ultrasonic measurements

rations coincide with the effective medium model by Ecker *et al.* (1998) and Helgerud *et al.* (1999). P-wave velocities follow the trend of the pore-filling model but show higher values. We attribute these higher values to the partial cementing of grains by THF hydrate. The effective medium models show end members of possible hydrate distributions. A mixing of hydrate suspended in the pore fluid with hydrate partially cementing the grains is possible. This behavior has been described by Fabricius (2003) as IF (isoframe) models. While the hydrate is entirely pore filling at low saturations it starts to cement the grain surfaces at higher saturations.

CONCLUSION

MXCT images show that hydrate forms in the pores as part of the pore fluid and as cement. Acoustic velocities increase only after cooling the sample well below hydrate stability temperature. We conclude that hydrate first forms in the pore space. Acoustic velocities increase only after hydrate saturation increases enough to form cements. Our results show that a significant amount of hydrate might remain undetected by seismic methods alone.

Given that THF hydrate is a proxy for one possible texture of natural occurring hydrate, we conclude that natural gas hydrate in coarse grained sediments is partially suspended in the pore fluid and partially load bearing when formed from natural gas dissolved in water. This conclusion is essential for the assessment of gas hydrate saturation from seismic and well log data.

ACKNOWLEDGMENTS

REFERENCES

Anderson, B. J., Wilder, J. W., Kurihara, M., White, M. D., Moridis, G. J., Wilson, S. J., Pooladi-Darvish, M., Masuda, Y., Collett, T. S., Hunter, R. B., *et al.* 2008. Analysis of modular dynamic formation test results from the Mount Elbert 01 stratigraphic test well, Milne Point Unit, North Slope, Alaska. *British Columbia, Canada.*

Boswell, R., and Collett, T. S. 2006. *Fire in the Ice: The gas hydrates resource pyramid.*

Chaouachi, M., Falenty, A., Sell, K., Enzmann, F., Kersten, M., Haberthr, D., and Kuhs, W. F. 2015. Microstructural evolution of gas hydrates in sedimentary matrices observed with synchrotron X-ray computed tomographic microscopy. *Geochemistry, Geophysics, Geosystems*, 1711–1722.

Collett, T. S., and Ladd, J. 2000. Detection of gas hydrate with downhole logs and assessment of gas hydrate concentrations (saturations) and gas volumes on the blake ridge with electrical resistivity log data. **164**, 179–191.

Collett, T. S., and Lee, M. W. 2012. Well Log Characterization of Natural Gas Hydrates 1. **53**(5), 348–367.

Collett, T. S, Johnson, A. H., Knapp, C. C., and Boswell, R. 2009. Natural Gas Hydrates: A Review. *Natural gas hydrates - Energy resource potential and associated geologic hazards: AAPG Memoir*, **89**, 146–219.

Dallimore, S. R., Wright, J. F., Nixon, F. M., Kurihara, M., Yamamoto, K., Fuji, K., Numasawa, M., Yasuda, M., and Imasato, Y. 2008. Geologic and porous media factors affecting the 2007 production response characteristics of the JOGMEC/NRCAN/AURORA Mallik gas hydrate production research well.

Dobrynin, V. M., Korotajev, Yu. P., and Plyuschev, D. V. 1981. *Gas hydrates - a possible energy resource*. Pitman Publishers, Boston.

Ecker, C., Dvorkin, J., and Nur, A. 1998. Sediments with gas hydrates: Internal structure from seismic AVO. *Geophysics*, **63**(5), 1659–1669.

Fabricius, I. L. 2003. How burial diagenesis of chalk sediments controls sonic velocity and porosity. *AAPG Bulletin*, **87**(11), 1755–1778.

Helgerud, M. B., Dvorkin, J., Nur, A., Sakai, A., and Collett, T. S. 1999. Elastic-wave velocity in marine sediments with gas hydrates: Effective medium modeling. *Geophysical Research Letters*, **26**(13), 2021–2024.

Kerkar, P. B., Jones, K. W., Kleinberg, R., Lindquist, W. B., Tomov, S., Feng, H., and Mahajan, D. 2009. Direct observations of three dimensional growth of hydrates hosted in porous media. *Applied Physics Letters*, **95**(2), 024102.

Kerkar, P. B., Horvat, K., Jones, K. W., and Mahajan, D. 2014. Imaging methane hydrates growth dynamics in porous media using synchrotron X-ray computed microtomography. *Geochemistry, Geophysics, Geosystems*, **15**(12), 4759–4768.

Kunerth, D. C., Weinberg, D. M., Rector, J. W., Scott, C. L., and Johnson, J. T. 2001. Acoustic laboratory measurements during the formation of a THF-hydrate in unconsolidated porous media. *Journal of seismic exploration*, **9**(4), 337–354.

Lee, J. Y., Yun, T. S., Santamarina, J. C., and Ruppel, C. 2007. Observations related to tetrahydrofuran and methane hydrates for laboratory studies of hydrate-bearing sediments. *Geochemistry, Geophysics, Geosystems*, **8**(6).

Lide, D. R., and Frederikse, H. P. R. 1995. *CRC handbook of chemistry and physics*.

Makino, T., Sugahara, T., and Ohgaki, K. 2005. Stability boundaries of tetrahydrofuran+ water system. *Journal of Chemical & Engineering Data*, **50**(6), 2058–2060.

Meyer, R. F. 1981. Speculations on oil and gas resources in small fields and unconventional deposits. *Long-term Energy Resources*, **1**, 49–72.

Pearson, C., Murphy, J., and Hermes, R. 1986. Acoustic and resistivity measurements on rock samples containing tetrahydrofuran hydrates: laboratory analogues to natural gas hydrate deposits. *Journal of Geophysical Research: Solid Earth*, **91**(B14), 14132–14138.

Priest, J. A., Best, A. I., and Clayton, C. R. I. 2005. A laboratory investigation into the seismic velocities of methane gas hydrate-bearing sand. *Journal of Geophysical Research: Solid Earth*, **110**(B4).

Rydzy, M. B., and Batzle, M. L. 2011. Rock physics characterization of THF hydrate-bearing sediment. *In: Proceedings of the 7th International Conference on Gas Hydrates*.

Schindler, M., and Batzle, M. L. 2014. Pore-Scale Investigation of Hydrate-Bearing Sediments. *In:* Poate, J. M., Kazemi H. Illangasekare T. H. Kee R. J. (ed), *Pore Scale Phenomena - Frontiers in Energy and Environment*. Golden, Colorado, USA: World Scientific.

Sloan, E. D., and Koh, C. A. 2008. *Clathrate hydrates of natural gases*. CRC press.

Spangenberg, E., Kulenkampff, J., Naumann, R., and Erzinger, J. 2005. Pore space hydrate formation in a glass bead sample from methane dissolved in water. *Geophysical Research Letters*, **32**(24).

Van Geet, M., Swennen, R., and Wevers, M. 2000. Quantitative analysis of reservoir rocks by microfocus X-ray computerised tomography. *Sedimentary Geology*, **132**(1-2), 25–36.

Waite, William F., Winters, William J., and Mason, D. H. 2004. Methane hydrate formation in partially water-saturated Ottawa sand. *American Mineralogist*, **89**(8-9), 1202–1207.

Yun, T. S., Francisca, F. M., Santamarina, J. C., and Ruppel, C. 2005. Compressional and shear wave velocities in uncemented sediment containing gas hydrate. *Geophysical Research Letters*, **32**(10).